



THE UNIVERSITY *of* EDINBURGH

Edinburgh Research Explorer

## Assessing the impact of diagenesis on foraminiferal geochemistry from a low latitude, shallow-water drift deposit

### Citation for published version:

Stainbank, S, Spezzaferri, S, De Boever, E, Bouvier, A-S, Chilcott, C, de Leau, E, Foubert, A, Kunkelova, T, Pichevin, L, Raddatz, J, Rüggeberg, A, Wright, JD, Yu, SM, Zhang, M & Kroon, D 2020, 'Assessing the impact of diagenesis on foraminiferal geochemistry from a low latitude, shallow-water drift deposit', *Earth and Planetary Science Letters*, vol. 545, pp. 116390. <https://doi.org/10.1016/j.epsl.2020.116390>

### Digital Object Identifier (DOI):

[10.1016/j.epsl.2020.116390](https://doi.org/10.1016/j.epsl.2020.116390)

### Link:

[Link to publication record in Edinburgh Research Explorer](#)

### Document Version:

Peer reviewed version

### Published In:

Earth and Planetary Science Letters

### General rights

Copyright for the publications made accessible via the Edinburgh Research Explorer is retained by the author(s) and / or other copyright owners and it is a condition of accessing these publications that users recognise and abide by the legal requirements associated with these rights.

### Take down policy

The University of Edinburgh has made every reasonable effort to ensure that Edinburgh Research Explorer content complies with UK legislation. If you believe that the public display of this file breaches copyright please contact [openaccess@ed.ac.uk](mailto:openaccess@ed.ac.uk) providing details, and we will remove access to the work immediately and investigate your claim.



1 **Assessing the impact of diagenesis on foraminiferal geochemistry from a low latitude,**  
2 **shallow-water drift deposit**

3  
4 Stephanie Stainbank<sup>a</sup>, Silvia Spezzaferri<sup>a</sup>, Eva De Boever<sup>a,1</sup>, Anne-Sophie Bouvier<sup>b</sup>, Colin  
5 Chilcott<sup>c</sup>, Erica S de Leau<sup>c</sup>, Anneleen Foubert<sup>a</sup>, Tereza Kunkelova<sup>c,2</sup>, Laetitia Pichevin<sup>c</sup>, Jacek  
6 Raddatz<sup>d,e</sup>, Andres Rüggeberg<sup>a</sup>, James D Wright<sup>f</sup>, Siyao M Yu<sup>f</sup>, Manlin Zhang<sup>c,3</sup>, Dick Kroon<sup>c</sup>

7  
8 <sup>a</sup>Department of Geosciences, University of Fribourg, Chemin du Musée 6, 1700 Fribourg,  
9 Switzerland

10 <sup>b</sup>Institute of Earth Sciences, University of Lausanne, Géopolis, 1015 Lausanne, Switzerland

11 <sup>c</sup>School of GeoSciences, University of Edinburgh, Grant Institute, The King's Buildings,  
12 James Hutton Road, EH9 3FE Edinburgh, United Kingdom

13 <sup>d</sup>Institute of Geosciences, Goethe University Frankfurt, Altenhöferallee 1, 60438 Frankfurt,  
14 Germany

15 <sup>e</sup>Frankfurt Isotope and Element Research Center (FIERCE), Goethe University Frankfurt,  
16 Altenhöferallee 1, 60438 Frankfurt, Germany

17 <sup>f</sup>Department of Earth and Planetary Sciences, Rutgers, the State University of New Jersey,  
18 Bush Campus, 610 Taylor Road, Piscataway, NJ 08854-8066, USA

19

20 <sup>1</sup>Present address: TNO, Geological Survey of the Netherlands, Princetonlaan 6, 3584 CB  
21 Utrecht, the Netherlands

22 <sup>2</sup>Present address: National Oceanography Centre Southampton, University of Southampton,  
23 Waterfront Campus, European Way, SO14 3ZH Southampton, United Kingdom

24 <sup>3</sup>Present address: Faculty of Life Science, University of Bradford, Richmond Rd, BD7 1DP  
25 Bradford, United Kingdom

26

27 Corresponding author e-mail: stephanie.hayman@unifr.ch

28

29

30 Key words: foraminifera; early diagenesis; tropical drift deposits; stable isotopes; Mg/Ca;  
31 IODP

32

33

34 **ABSTRACT**

35 Due to their large heat and moisture storage capabilities, the tropics are fundamental in  
36 modulating both regional and global climate. Furthermore, their thermal response during past  
37 extreme warming periods, such as super interglacials, is not fully resolved. In this regard, we  
38 present high-resolution (analytical) foraminiferal geochemical ( $\delta^{18}\text{O}$  and Mg/Ca) records for  
39 the last 1800 kyr from the shallow (487 m) Inner Sea drift deposits of the Maldives  
40 archipelago in the equatorial Indian Ocean. Considering the diagenetic susceptibility of these  
41 proxies, in carbonate-rich environments, we assess the integrity of a suite of commonly used  
42 planktonic and benthic foraminifera geochemical datasets (*Globigerinoides ruber* (white),  
43 *Globigerinita glutinata* (with bulla), *Pulleniatina obliquiloculata* (with cortex) and *Cibicides*  
44 *mabahethi*) and their use for future paleoceanographic reconstructions.

45

46 Using a combination of spot Secondary Ion Mass Spectrometer, Electron Probe Micro-  
47 Analyzer and Scanning Electron Microscope image data, it is evident that authigenic  
48 overgrowths are present on both the external and internal test (shell) surfaces, yet the degree  
49 down-core as well as the associated bias is shown to be variable across the investigated  
50 species and proxies. Given the elevated authigenic overgrowth Mg/Ca (~12–22 mmol/mol)  
51 and  $\delta^{18}\text{O}$  values (closer to the benthic isotopic compositions) the whole-test planktonic *G.*  
52 *ruber* (w) geochemical records are notably impacted beyond ~627.4 ka (24.7 mcd). Yet,  
53 considering the setting (i.e. bottom water location) for overgrowth formation, the benthic  
54 foraminifera  $\delta^{18}\text{O}$  record is markedly less impacted with only minor diagenetic alteration  
55 beyond ~790.0 ka (28.7 mcd). Even though only the top of the *G. ruber* (w) and *C. mabahethi*  
56 records (whole-test data) would be suitable for paleo-reconstructions of absolute values (i.e.  
57 sea surface temperature, salinity, seawater  $\delta^{18}\text{O}$ ), the long-term cycles, while dampened,  
58 appear to be preserved. Furthermore, planktonic species with thicker-tests (i.e. *P.*

59 *obliquiloculata* (w/c)) might be better suited, in comparison to thinner-test counter-parts (i.e.  
60 *G. glutinata* (w/b), *G. ruber* (w)), for traditional whole-test geochemical studies in shallow,  
61 carbonate-rich environments. A thicker test equates to a smaller overall bias from the  
62 authigenic overgrowth. Overall, if the diagenetic impact is constrained, as done in this study,  
63 these types of diagenetically altered geochemical records can still significantly contribute to  
64 studies relating to past tropical seawater temperatures, latitudinal scale ocean current shifts  
65 and South Asian Monsoon dynamics.

66

67

68

69

70

71

72

73

74

75

76

77

78

79

80

81

82

83

84 **1. INTRODUCTION**

85 In comparison to deep-sea records, high-resolution (both temporal and analytical)  
86 paleoclimate reconstructions for shallow-intermediate, equatorial regions are limited. This is  
87 in part due to (i) the drive to reconstruct and model past global ocean circulation patterns,  
88 which predominantly use high-temporally resolved deep-sea archives, and which are difficult  
89 to recover from lower latitudes and (ii) the increased susceptibility of calcifying organisms to  
90 diagenetic overprint in shallow, carbonate-rich environments. The tropics are an integral  
91 component of both regional and global climatic systems due to their heat and moisture storage  
92 capabilities (Gupta et al., 2010 and references within; Hastenrath et al., 1993; Schott et al.,  
93 2009). Yet, notably there is a lack of reliable sea surface temperature (SST) and  $\delta^{18}\text{O}$  records  
94 from these equatorial regions, particularly from past extreme warming periods, which would  
95 further facilitate the understanding of tropical climatic systems. In this regard, we present a  
96 new high-resolution (analytical) tropical record from the Inner Sea of the Maldives  
97 archipelago in the equatorial Indian Ocean. We test the suitability of this unique tropical  
98 record for paleo-reconstructions given its shallow location, proximity to carbonate banks and  
99 the anticipated diagenetic alteration down-core.

100

101 Innumerable studies have shown that the geochemistry of foraminiferal tests (shells) are  
102 invaluable paleoceanographic, -climatic and -ecological archives (e.g. Birch et al., 2013;  
103 Kroon and Ganssen, 1989; Lisiecki and Raymo, 2005; Groeneveld et al., 2008; Raddatz et al.,  
104 2017; Stainbank et al., 2019). Yet, many of these geochemical proxies (e.g. Mg/Ca and  $\delta^{18}\text{O}$ )  
105 are susceptible to diagenetic alteration, which calls into question their fidelity (Edgar et al.,  
106 2015, 2013; Groeneveld et al., 2008; Panieri et al., 2017). According to Edgar et al. (2015) the  
107 foraminifera test wall, texture and morphology are prone to at least three diagenetic processes:  
108 overgrowth, partial dissolution and recrystallization. All three have the potential to bias the

109 original test geochemistry and affect the accuracy of paleo-reconstructions. As such, prior to  
110 undertaking paleo-reconstructions, it is paramount to establish the diagenetic state of this  
111 foraminiferal calcite. This is particularly important within carbonate-rich environments which  
112 have high sediment porosity and permeability and thus a higher “diagenetic potential” in  
113 comparison to the more impermeable clay-rich sediments (Edgar et al., 2013). Additionally,  
114 in comparison to the more robust, heavily calcified benthic foraminifera, planktonic tests are  
115 more susceptible to alteration (Edgar et al., 2013). Moreover, as there is a large array of  
116 planktonic foraminifera test wall textures; this influence is not necessarily uniform between  
117 species. Bé (1977) correlated increased diagenetic resistance for species with smaller pores,  
118 thicker walls and larger test size. These considerations are important to aid in the selection of  
119 less diagenetically predisposed foraminiferal species, particularly for depth stratified (i.e.  
120 studies assessing discrete living and calcification depths within the water column) thermocline  
121 reconstructions.

122

123 To contribute to an improved understanding of ocean-atmospheric interactions within the  
124 tropical Indian Ocean, and the associated foraminiferal diagenetic processes, we present high  
125 analytically resolved foraminiferal datasets from the shallow, Maldives Inner Sea.

126 Specifically, our study addresses the following issues: (i) the overall preservation state of the  
127 individual long-term geochemical records and their suitability for future paleoceanographic  
128 interpretations and (ii) the differential susceptibility to diagenesis for three planktonic  
129 foraminiferal species, with discrete wall textures, and a benthic counterpart using a  
130 combination of imaging and elemental/isotopic geochemical approaches.

131

## 132 **2. METHODS**

133 This study uses samples retrieved during the International Ocean Discovery Program (IODP)  
134 Expedition 359 in 2015. All samples come from Site U1467 (4°51.0274'N, 73°17.0223'E)  
135 drilled at a water depth of 487 m within the drift deposits of the Inner Sea of the Maldives  
136 archipelago in the northern equatorial Indian Ocean (Fig. 1) (Betzler et al., 2017). The base of  
137 these drift deposits have been biostratigraphically dated to 12.9-13.0 Ma, coinciding with the  
138 establishment of the South Asian Monsoon (Betzler et al., 2018, 2016). As such, the drift  
139 deposits represent an important paleoceanographic and -monsoon archive due to their unique  
140 ability to preserve continuous sediment records by bottom current deposition (Lüdmann et al.,  
141 2013). The top 61 meters composite depth (mcd) from Hole U1467B, C, composed of  
142 unlithified foraminifer-rich wackestone to packstone, were used in this study. The shipboard  
143 splice was adjusted after the Expedition based on X-ray fluorescence core scanner data using  
144 Fe intensity (counts per second, cps) (Kunkelova et al., 2018).

145

146 **Fig. 1. Study location and position of IODP Expedition 359 Site U1467 in the Inner Sea**  
147 **of the Maldives (blue circle), located in the northern equatorial Indian Ocean (GEBCO**  
148 **Compilation Group, 2019).**

149

150 Long-term, high-resolution (analytical) whole-test (whole-shell) stable isotopic ( $\delta^{18}\text{O}$ ) records  
151 are compiled for three planktonic species, *Globigerinoides ruber* (white), *Globigerinita*  
152 *glutinata* (with bulla), *Pulleniatina obliquiloculata* (with cortex) and one benthic  
153 representative *Cibicides mabahethi*. In a few cases when the target benthic species is rare,  
154 *Cibicides wuellerstorfi* tests are included to ensure enough calcite for the isotopic  
155 measurements. Complementary whole-test Mg/Ca ratios are measured for *G. ruber* (w).

156

157 A combination of methods is utilized to constrain the influence and susceptibility of  
158 diagenetic alteration on the foraminiferal test geochemistry. A visual Scanning Electron  
159 Microscope (SEM) check is implemented, on selected samples, for both the target planktonic  
160 and benthic species. This visual check is then used to define a qualitative Diagenesis Rank  
161 (DR) to ascertain and track the down-core change in the preservation state of the foraminiferal  
162 tests. Supplementary spot-geochemical (isotopic and elemental) measurements are obtained  
163 using a Secondary Ion Mass Spectrometer (SIMS) and Electron Probe Micro-Analyzer  
164 (EPMA).

165

### 166 **2.1. Site U1467 mineralogy and geochemistry**

167 Site U1467 sediment core interstitial water chemistry and sediment mineralogy are presented  
168 in Betzler et al. (2017). Concentrations of  $\text{Ca}^{2+}$ ,  $\text{Mg}^{2+}$  and  $\text{Sr}^{2+}$  were measured from interstitial  
169 water (IW) samples either by shipboard Inductively Coupled Plasma Atomic Emission  
170 Spectroscopy (ICP-AES) or shore-based ion chromatography (see Betzler et al., 2017; Blättler  
171 et al., 2019 for further details). Relative concentrations of aragonite, high-Mg calcite (HMC),  
172 low-Mg calcite (LMC), dolomite, and quartz were measured using X-ray powder diffraction  
173 (XRD) (see Betzler et al., 2017 for a full overview of the data collection methods). For  
174 simplicity we show only the data, reported as mbsf (meters below seafloor), from Hole  
175 U1467B as it yielded the most extensive and intact records at this site (Fig. 2).

176

177 **Fig. 2. IODP Expedition 359 Hole U1467B sediment mineralogy and pore water**  
178 **geochemistry** (Betzler et al., 2017).

179

### 180 **2.2. Species selection criteria**



181 To explore the susceptibility of different species to diagenetic alteration and the biases on  
182 their respective whole-test geochemical compositions, we assess three shallow/intermediate  
183 dwelling planktonic foraminiferal species: *G. ruber* (w), *G. glutinata* (w/b) and *P.*  
184 *obliquiloculata* (w/c). These species have reported apparent calcification depths for the  
185 northern equatorial Indian Ocean of ~70 m, 81 m and 74–104 m, respectively (Stainbank et  
186 al., 2019) and have discrete wall textures, thicknesses and porosities (Supplementary Material  
187 1). *Globigerinoides ruber* (w) is chosen as it is the predominant foraminiferal species used for  
188 surface/near-surface seawater reconstructions (e.g. Birch et al., 2013; Bunzel et al., 2017;  
189 Rebotim et al., 2017; Stainbank et al., 2019). *Globigerinoides ruber* (w) is a spinose,  
190 shallow-dweller with a cancellate wall texture and a porosity of ~5 pores/25 x 25  $\mu\text{m}$  (Bé,  
191 1968) (Supplementary Material 1). *Globigerinita glutinata* (w/b) is included as a second  
192 shallow-dweller, as it is non-spinose with a smooth, microperforate wall texture with a  
193 porosity of ~112 pores/25 x 25  $\mu\text{m}$  (Bé, 1968; Birch et al., 2013; Stainbank et al., 2019)  
194 (Supplementary Material 1). Lastly, the shallow-intermediate dweller *P. obliquiloculata* (w/c)  
195 is included as it is non-spinose, with a smooth wall texture (Birch et al., 2013; Stainbank et  
196 al., 2019). While the original test has a porosity of ~9 pores/25 x 25  $\mu\text{m}$ , the formation of the  
197 smooth, glossy cortex layer drastically reduces the diameter and spherical nature of the pores  
198 resulting in a reduction in the overall porosity (Bé, 1968; Steinhardt et al., 2015)  
199 (Supplementary Material 1). *Cibicides mabahethi*, a calcareous hyaline epibenthic species, is  
200 chosen as the benthic representative for this site as it has been shown to accurately record  
201 bottom water conditions for the first ~200 kyr (time interval of the study by Bunzel et al.,  
202 2017) for the Maldives Inner Sea (Bunzel et al., 2017).

203

### 204 **2.3. Traditional whole-test foraminiferal geochemical analysis**

205 Sediment samples were air dried, weighed and washed through a 32  $\mu\text{m}$  sieve to remove the  
206 finer silts and clay fraction. They were then oven-dried at 30°C for 48 hours, weighed and dry  
207 sieved into discrete fractions for foraminiferal picking. For all geochemical analyses, species  
208 were picked from pre-defined, narrow sieve size fractions, to minimize intra-specific  
209 ontogenetic isotopic fractionation effects (Stainbank et al., 2019). Additionally, to remove any  
210 adhering particles, and to prevent carbonate contamination, all picked specimens were  
211 precleaned in Milli-Q water for a few seconds by ultrasonication.

212  
213 In total, 3802 traditional whole-test stable oxygen isotopic ( $\delta^{18}\text{O}$ ) measurements were made  
214 (data is available on Pangaea). From 0–61 mcd a measurement for *G. ruber* (w: 212–250  $\mu\text{m}$ )  
215 was obtained every  $\sim$ 3 cm. Isotopic analyses of *G. glutinata* (w/b: 125–150  $\mu\text{m}$ ) and *P.*  
216 *obliquiloculata* (w/c: 355–400  $\mu\text{m}$ ), were carried out across three selected intervals with  
217 differential diagenetic influences (see Section 3.2 for more details) at a resolution of 3–12 cm;  
218 Interval 1 (15.2–20.5 mcd), Interval 2 (31.4–34.5 mcd) and Interval 3 (53.3–56.1 mcd).  
219 Benthic isotopic data (*C. mabahethi* > 180  $\mu\text{m}$ ) were only generated at a  $\sim$ 3 cm resolution  
220 between 0–40.0 mcd as below this interval they become scarce. The *G. ruber* (w) and *C.*  
221 *mabahethi*  $\delta^{18}\text{O}$  measurements for the top 6.7 mcd (n = 441) were analyzed at Rutgers  
222 University on a MicroMass (FISONS) Optima Isotope Ratio Mass Spectrometer with an  
223 attached multi-prep device. Samples were reacted with 100 % phosphoric acid ( $\text{H}_3\text{PO}_4$ ) at  
224 90°C for 15 min, and the evolved  $\text{CO}_2$  gas collected in a liquid nitrogen coldfinger and  
225 analyzed compared to a reference gas. The samples are corrected using an internal laboratory  
226 standard (RGF1), which is routinely run against NBS-19 and NBS-18. All other  $\delta^{18}\text{O}$  data (n  
227 = 3361) were obtained at the Grant Institute of the University of Edinburgh on a Thermo  
228 Electron Delta+ Advantage Mass Spectrometer integrated with a Kiel carbonate III automated  
229 extraction line and corrected using the laboratory's internal standard. Approximately 0.05 mg

230 was required for each measurement with each expressed as parts per mil (‰) relative to  
231 Vienna Pee Dee Belemnite (VPDB). Replicate measurements of the standards give the  
232 instruments an analytical precision ( $1\sigma$ ) of  $\sim 0.05$  ‰ for  $\delta^{18}\text{O}$  and  $\delta^{13}\text{C}$ . The reproducibility,  
233 based on inter-laboratory replicate measurements ( $n = 6$ ), was  $\sim 0.20$  ‰.

234

235 Mg/Ca ratios were measured on 30 pooled *G. ruber* (w: 212–250  $\mu\text{m}$ ) tests from a sample  
236 every  $\sim 3$  cm, for the interval 14.8–31.4 mcd ( $n = 535$ ; data is available on Pangaea). All  
237 samples were cleaned according to the standard oxidative protocol of Barker et al. (2003).  
238 Samples were then leached with a very weak 0.001N  $\text{HNO}_3$  acid solution prior to dissolving  
239 in 0.075M  $\text{HNO}_3$ . The reductive cleaning step was excluded as it has been shown to cause the  
240 dissolution of the foraminiferal tests resulting in subsequently lower Mg/Ca values (Barker et  
241 al., 2003; Elderfield et al., 2006). Analyses were conducted at the Institute of Geosciences of  
242 the Goethe University of Frankfurt and at the School of GeoSciences at the University of  
243 Edinburgh. The former measurements ( $n = 232$ ) were carried out by Inductively Coupled  
244 Plasma Optical Emission Spectrometry (ICP-OES) on a Thermoscientific iCap 6300 (dual  
245 viewing) and the latter ( $n = 303$ ) on a Vista Pro ICP-OES. Inter-laboratory replicates ( $n = 11$ )  
246 were run to assess potential differences and the reproducibility which was determined to be  
247 better than 0.30 mmol/mol (mean difference). In Frankfurt, the final centrifuged sample  
248 solutions were diluted with an yttrium solution (1 mg/l) prior to measurement to allow for the  
249 correction of matrix effects. Whereas, in Edinburgh a set of six standard solutions (with  
250 increasing Ca concentrations from 0 to 100 %) were used for matrix and background  
251 correction (Sadekov et al., 2013). At both facilities, five calibration solutions were measured  
252 before each analysis to allow for intensity ratio calibrations. Element/Ca measurements were  
253 standardized using an internal consistency standard (ECRM 752-1, 3.761 mmol/mol Mg/Ca).  
254 Replicates of the ECRM at the Edinburgh ( $n = 61$ ) and Frankfurt ( $n = 45$ ) facilities yielded  $2\sigma$

255 Mg/Ca uncertainties (SD) of 0.15 and 0.17 mmol/mol, respectively. During all Mg/Ca  
256 measurements, the elements Al, Fe, and Mn were screened to check for Mn-Fe oxide coatings  
257 and clay mineral contamination. Procedural blanks were routinely run to monitor for potential  
258 contamination during the cleaning process.

259

#### 260 **2.4. Electron Probe Micro-Analyzer (EPMA) analysis**

261 Samples for both EPMA and SIMS (Section 2.5) analyses were selected to provide  
262 representatives from the entire length of core including altered versus non-altered portions  
263 (see Section 3.2 for sample locations). Polished cross-sections of *G. ruber* (w) (n = 36) and *P.*  
264 *obliquiloculata* (w/c) (n = 6) tests were prepared by embedding the tests in Struers Epothin.  
265 Briefly, selected tests were (i) cleaned according to the same oxidative protocol (Barker et al.,  
266 2003) as for the traditional whole-test Mg/Ca geochemical analyses and (ii) placed umbilical  
267 side-down on adhesive film within 1-inch Struers mounting cups, then (iii) embedded in  
268 Epothin and degassed under high vacuum for 5 minutes and once set (iv) polished using a  
269 successively finer Struers water-based diamond suspension from 9  $\mu\text{m}$  down to 0.25  $\mu\text{m}$  to  
270 expose a cross-section of each test (Supplementary Material 2). All EPMA samples were then  
271 coated in 5 nm of carbon.

272

273 Quantitative Mg and Ca spot analyses and semi-quantitative elemental maps were measured  
274 using a JEOL JXA-8530F Electron Probe Micro-Analyzer, equipped with a Schottky field  
275 emission gun, at the Faculty of Geosciences and Environment of the University of Lausanne.  
276 Calcite,  $\text{CaCO}_3$  (Ca = 39.98 wt%) and dolomite,  $\text{CaMg}(\text{CO}_3)_2$  (Mg = 13.18 wt%) were used  
277 as standards for Ca and Mg, respectively. Spot measurements were acquired using a 10 kV  
278 accelerating voltage and probe size of 1–2  $\mu\text{m}$ . Overview elemental maps were carried out  
279 with a 0.50  $\mu\text{m}$  step size, an image resolution of 720  $\times$  600 pixels, 7 kV accelerating voltage,

280 an electron beam current of 10 nA and a dwell time of 50 ms. Additional higher resolution  
281 elemental maps were obtained with a 0.23–0.29  $\mu\text{m}$  step size and an image resolution of  
282 256 $\times$ 192 pixels.

283

## 284 **2.5. Secondary Ion Mass Spectrometer (SIMS) analysis**

285 Polished cross sections, of selected *G. ruber* individuals ( $n = 27$ ) were prepared for SIMS  
286 analyses following the same protocol as for the EPMA samples (Section 2.4), with the  
287 exclusion of the initial oxidative cleaning step. *In situ* oxygen isotope analyses were carried  
288 out using a Cameca IMS 1280-HR Secondary Ion Mass Spectrometer (SIMS) at the  
289 SwissSIMS ion probe facility within the University of Lausanne (Supplementary Material 3).  
290 A primary  $\text{Cs}^+$  ion beam with an intensity of 1.2nA was focused to a size of  $\sim 10 \mu\text{m}$ . The  
291 secondary  $^{16}\text{O}$  and  $^{18}\text{O}$  were detected simultaneously on two faraday cups, which were  
292 calibrated at the beginning of the session. The mass resolving power was set to 2400 (entrance  
293 slit set at 121  $\mu\text{m}$  and multicollection slit 1), in order to fully remove possible  $^{17}\text{OH}$   
294 interference on mass 18. A single analysis took  $\sim 4$  min, including 30 sec. of pre-sputtering,  
295 automatic centering of secondary deflectors and 20 cycles of 5 sec. of measurements.  
296 Calibration was made using an in-house pure calcite standard (UNIL-C1). Six analyses of the  
297 standard were made at the beginning of the measurements for each mount, after which UNIL-  
298 C1 was measured once every four analyses. Reproducibility of the standard (spot to spot) was  
299 0.4 and 0.3 ‰ ( $2\sigma$ ) on the two mounts, respectively. Internal uncertainty (single analysis) was  
300 0.3 to 0.4 ‰ ( $2\sigma$ ).

301

## 302 **2.6. Scanning Electron Microscopy (SEM)**

303 Thirty-five samples from the top 61 mcd of the core are used to constrain the preservation  
304 state of the target planktonic and benthic foraminiferal species. Samples are positioned at

305 regular intervals down-core and include representatives from glacial and interglacial peaks  
306 (see Section 3.2 for sample locations). From each sample, three to four *G. ruber* (w), *G.*  
307 *glutinata* (w/b), *P. obliquiloculata* (w/c) and *C. mabahethi/wuellerstorfi* tests were picked  
308 from the same size fractions as used for the geochemical analyses. Tests were cleaned for a  
309 few seconds by ultrasonication in Milli-Q water, cracked open and mounted on carbon based  
310 adhesive discs on standard SEM stubs. Stubs were coated, under vacuum, in 40 nm of gold  
311 using a Bal-tec SCD 050 sputter coater and imaged on a Thermo Fisher SEM FEIXL30SFEG.  
312 The preservation state of each species for each sample is ascertained, using SEM images,  
313 according to three categories (i) external test surface, (ii) internal test surface and (iii) test  
314 wall texture (Table 1). A ranking is assigned for each category and the sum (total out of 7)  
315 used to define the overall qualitative Diagenesis Rank (DR) for each species, with 0 defining  
316 ‘pristine tests’ and 7 the most ‘diagenetically altered’.

317

318 **Table 1. Diagenesis Rank categories and classifications.**

Ranking	Category		
	1. External surface	2. Internal surface	3. Wall texture
0	Pristine unaltered surface texture with no authigenic overgrowth crystals present both on the test surface or within the pores		Pristine microgranular wall texture with well-defined pores
1	Small overgrowths present (up to ~0.5 $\mu\text{m}$ ) with a patchy-uniform distribution		Visibly altered wall texture with authigenic crystals within the wall cross sections either due to overgrowth precipitation or partial recrystallization
2	Mostly medium sized overgrowths present (~0.5-2 $\mu\text{m}$ ) with a uniform distribution		
3	Mostly large sized overgrowths present (>2 $\mu\text{m}$ ) with a uniform distribution		

319

320 Using the MATLAB v2018a software, a color-map is generated for each species to visualize  
321 the down-core evolution in preservation state (i.e. the change in DR). The 35 samples are used  
322 to define an initial matrix, and the rankings interpolated between each point using a linear  
323 function.

324

## 325 **2.7. Age model**

326 The stratigraphic framework for the upper 61 mcd of Site U1467 is established by graphically  
327 correlating both our planktonic *G. ruber* (w) and benthic *C. mabahethi*  $\delta^{18}\text{O}$  records to the  
328 stacked reference curve of Ahn et al. (2017) (Prob-stack). Prob-stack was selected as it is  
329 based on a compilation of 180 global benthic isotope records and includes the datasets from  
330 the frequently used LR04  $\delta^{18}\text{O}$  stack of Lisiecki and Raymo (2005). The age model for our  
331 datasets is obtained using Analyseries v2.0.4 (Paillard et al., 1996). To facilitate the tuning  
332 process, initially all datasets were linearly detrended and our planktonic and benthic records  
333 smoothed (3 pt. running average) to eliminate some of the noise. The main glacial and  
334 interglacial peaks are used as the initial tie-points, with additional prominent maxima and  
335 minima subsequently correlated to optimize the visual alignment of the datasets  
336 (Supplementary Material 4).

337

## 338 **3. RESULTS**

### 339 **3.1. Carbonate mineralogy**

340 At IODP Expedition 359 Hole U1467B, LMC is ubiquitous, generally contributed by  
341 planktonic foraminifera and coccoliths, making up the bulk of the sediment mineralogy from  
342 the core-top down to 700 mbsf (Fig. 2, Betzler et al., 2017). Aragonite is contributed mainly  
343 by *Halimeda* fragments, coral fragments and pteropods, and decreases from ~46 % between  
344 0–10 mbsf to only 9 % at 200 mbsf. From 200 to 500 mbsf aragonite still has a small, variable  
345 contribution (0–9 %). However, a marked increase in the aragonite contribution is noted from  
346 500–600 mbsf (up to 23 %) with again a decrease down to 700 mbsf. HMC (with  $\text{Mg}^{2+}$   
347 concentrations  $>4$  mol%; Morse, 2003), which is contributed predominantly by red coralline  
348 algae, benthic foraminifera, bryozoans, and echinoderms, is only present (4–7 %) in the

349 sediments in the top 10 mbsf. Minor peaks in dolomite mainly occur within the top 400 mbsf.  
350 The pore-fluid species ( $\text{Ca}^{2+}$ ,  $\text{Mg}^{2+}$  and  $\text{Sr}^{2+}$ ) are visibly correlated with the aragonite  
351 concentrations (Betzler et al., 2017). Both  $\text{Ca}^{2+}$  and  $\text{Mg}^{2+}$  respectively, increase and decrease  
352 concomitantly with a reduction in aragonite percent contribution.  $\text{Sr}^{2+}$  increases rapidly to  
353 peak concentrations around 100 mbsf where it plateaus until ~500 mbsf below which there is  
354 a gradual decline.

355

356 The study interval (0 to ~61 mbsf), corresponds to Unit I (0–110 mbsf) of the logged  
357 lithostratigraphic units (a total of 6 units were identified) at Site U1467 (Betzler et al., 2017).  
358 It consists of an unlithified foraminifer-rich wackestone to packstone (very fine to fine  
359 grained) with a calcareous ooze matrix (Betzler et al., 2017). As noted, the abundance of  
360 aragonite is high in the study interval with HMC present in the first 10 mbsf. The species  $\text{Ca}^{2+}$   
361 and  $\text{Sr}^{2+}$  are present in their lowest concentrations (mean  $\text{Ca}^{2+}$ : 10.61 mM,  $\text{Sr}^{2+}$  111.42 mM)  
362 whereas,  $\text{Mg}^{2+}$  is in its highest concentration (mean  $\text{Mg}^{2+}$ : 53.58 mM) (Betzler et al., 2017).

363

### 364 **3.2. Traditional whole-test foraminiferal geochemistry and Diagenesis Ranks**

365 All geochemical records ( $\delta^{18}\text{O}$  and  $\text{Mg}/\text{Ca}$ ) show clear cyclicity down-core (Figs. 3-4). Based  
366 on the alignment of the stable isotope stratigraphies, the planktonic  $\delta^{18}\text{O}$  *G. ruber* (w) record  
367 from 0–61.0 mcd represents the time interval 0–1800.0 kyr covering Marine Isotope Stage  
368 (MIS) 1-64 (Figs. 3a, 4a-b). The benthic record, spanning 0–40.0 mcd, encompasses the  
369 interval 0 to 1179.0 kyr (Figs. 3c, 4a,c), MIS1-35. The sedimentation rate varies down-core  
370 between 0.4–16.3 cm/kyr (Fig. 4d).

371

372 **Fig. 3. Long-term geochemical records from IODP Expedition 359 Site U1467 against**  
373 **core depth with (a) the *G. ruber* (w)  $\delta^{18}\text{O}$ , (b)  $\text{Mg}/\text{Ca}$  records and (c) the *C. mabahethi***



374  $\delta^{18}\text{O}$  record. Visual SEM check (grey circles) and EPMA/SIMS (red and black circles,  
375 respectively) samples are shown for reference. A 3-pt moving average smoothing was  
376 applied to our datasets (thick lines) to highlight the cycles.

377

378 **Fig. 4. (a) The benthic foraminifera  $\delta^{18}\text{O}$  stack (prob-stack) of Ahn et al. (2017) is used to**  
379 **obtain the age model for (b) IODP Expedition 359 Site U1467 *G. ruber* (w) and (c) *C.***  
380 ***mabahethi*  $\delta^{18}\text{O}$  records. A 3-pt moving average smoothing was applied to our datasets**  
381 **(b, c: thick lines) to highlight the cycles. Sedimentation rates (Sed. Rate) are referenced**  
382 **as cm/kyr in (d). Marine Isotope Stages (MIS) are shown (vertical dashed lines) and**  
383 **form the main tie-points for the age model (Supplementary Material 4).**

384

385 SEM observations reveal diagenetic alterations are primarily due to the precipitation of  
386 authigenic calcite (overgrowth) (Fig. 5). Furthermore, the diagenetic susceptibility of the four  
387 investigated species, *G. ruber* (w), *G. glutinata* (w/b), *P. obliquiloculata* (w/c) and *C.*  
388 *mabahethi*, differs down-core (Figs. 5-6). The resultant Diagenesis Rank (DR) values reflect a  
389 gradual decline, in the overall preservation state from 0 to 1800.0 kyr (0–61.0 mcd) (sample  
390 locations noted on Figs. 3, 6). While this down-core decline is variable across all species, all  
391 have pristine, unaltered tests in the core-top samples (359-U1467A, B-Mudline) (Fig. 5).  
392 Further down-core, authigenic overgrowths occur both on the internal and external test  
393 surfaces and within pores, resulting in a reduction in pore-size until complete infilling is  
394 achieved (Fig. 5, Supplementary Material 1). The size of these authigenic overgrowths varies  
395 from small and patchy to large (> 2  $\mu\text{m}$ ) well-developed, euhedral crystals growing  
396 perpendicular to the test wall and covering the entire inner and outer test surfaces  
397 (Supplementary Material 1).

398

399 **Fig. 5. Scanning Electron Microscope (SEM) images of (a) *G. ruber* (w), (b) *G. glutinata***  
400 **(w/b), (c) *P. obliquiloculata* (w/c) and (d) *C. mabahethi*/*C. wuellerstorfi* showing the outer**  
401 **(1, 2 and 4) and inner test surfaces (3, 5). Images of pristine IODP Expedition 359 Site**  
402 **U1467 tests from the core-top (Sample at 0 ka: A, B-Mudline) are shown in 1-3 and**  
403 **images of diagenetically altered tests (Sample at 1743.8 ka, 58.7 mcd: B-7H-3, 75-76 cm)**  
404 **are shown in 4-5. Representative examples of overgrowth size and distribution are**  
405 **shown for the inner test surfaces of *G. ruber* (w) in (e-h) (Samples: e. B-Mudline; f. B-**  
406 **3H-4, 99-100 cm; g. B-4H-5, 36-37 cm; h. C-6H-5, 57-58 cm). White bars show test wall**  
407 **thicknesses and red arrows indicate representative examples of overgrowth crystals.**  
408 **Whole-test scale bars = 100  $\mu$ m and close-up image scale bars = 20  $\mu$ m.**  
409

410 **Fig. 6. Long-term stable isotope ( $\delta^{18}\text{O}$ ) records for IODP Expedition 359 Site U1467 for**  
411 **(a) the planktonic species *G. ruber* (w) with intervals 1-3 comparing *G. glutinata* (w/b)**  
412 **and *P. obliquiloculata* (w/c) records (note: Selected Marine Isotope Stages (MIS) are**  
413 **shown for reference); Diagenesis Rank (DR) color maps are shown for (b) *G. ruber* (w),**  
414 **(c) *G. glutinata* (w/b), (d) *P. obliquiloculata* (w/c) and (e) *C. mabahethi* with (f) the long-**  
415 **term  $\delta^{18}\text{O}$  record for the benthic species *C. mabahethi*. The samples used for the visual**  
416 **SEM check are also shown as grey circles on (a). Red and teal curves show  $\delta^{18}\text{O}$  *G. ruber***  
417 **(w) and *C. mabahethi* data, respectively from Bunzel et al. (2017). A 3-pt moving average**  
418 **smoothing was applied to the datasets (thick lines) to highlight the cycles.**  
419

420 *Pulleniatina obliquiloculata* (w/c) appears to be the most susceptible species to authigenic  
421 overgrowth with medium sized, well-developed crystals already observed at ~274.5 ka (11.6  
422 mcd) on the external test surfaces. In contrast, these are first observed on *G. ruber* (w) at  
423 ~790.0 ka (28.7 mcd), *G. glutinata* (w/b) at ~558.3 ka (22.2 mcd) and the benthic tests further

424 down core at ~807.9 ka (29.1 mcd). Large well-developed authigenic crystals are evident on  
425 tests of *G. ruber* (w), *G. glutinata* (w/b), *P. obliquiloculata* (w/c) and *C. mabahethi* from  
426 ~1190.9 ka (40.6 mcd), ~1015.1 ka (36.0 mcd), ~864.7 ka (31.3 mcd) and ~872.0 ka (31.7),  
427 respectively (Supplementary Material 1). In addition to size, differences in overgrowth  
428 distributions are noted between the planktonic and benthic species. While all species show  
429 roughly similar development of overgrowth crystals across their outer test surface, with  
430 concentrations of overgrowths in the pores, distinct differences are observed on their inner  
431 test surfaces. For the planktonic species, authigenic overgrowths are more or less  
432 homogeneous across the surface whereas for the benthic species, they are generally  
433 concentrated within the pores and along the sutures with patchy growth across the inner  
434 surfaces (Supplementary Material 1).

435  
436 Intervals 1-3 were specifically selected, with reference to the *G. ruber* (w) DR data, as  
437 representative segments with differential diagenetic influences. Variability between the three  
438 planktonic  $\delta^{18}\text{O}$  records does occur across the intervals (Fig. 6). Interval 1, which covers  
439 MIS10-13 (354.0–505.0 kyr), has the lowest DR values for all species (0–3). Interval 2, which  
440 covers MIS21-26 (866.7–974.0 kyr), is located in the section with a notable increase in the  
441 respective DR values (2–4). Finally, Interval 3 covers MIS54-59 (1573.8–1690.9 kyr) in the  
442 most altered portion of the records with the highest DR values (> 4). The glacial-interglacial  
443 cycles are more prominent across all records in Interval 1. Both *G. ruber* (w) and *P.*  
444 *obliquiloculata* (w/c) display a large amplitude change from the glacial peak MIS12 across  
445 the deglaciation to the interglacial peak MIS11 ( $\Delta$  ~2.20 ‰ and 2.50 ‰, respectively).  
446 *Globigerinita glutinata* (w/b) shows a smaller change across MIS12 to MIS11 ( $\Delta$  1.41 ‰),  
447 and less prominent glacial-interglacial peaks in Interval 2 compared to *G. ruber* (w) and *P.*  
448 *obliquiloculata* (w/c). Interval 3 shows notably higher isotopic values with the glacial-

449 interglacial peaks markedly reduced, although still clearly visible, for all species. Despite the  
450 variation and extent of diagenetic alteration, Pleistocene glacial-interglacial cycles can be  
451 readily identified in all long-term  $\delta^{18}\text{O}$  records (Fig. 6). However, beyond  $\sim 1300$  ka (46.1  
452 mcd), the *G. ruber* (w) data shows a notable down-core trend towards higher  $\delta^{18}\text{O}$  values (Fig.  
453 6).

454

### 455 **3.3. Comparison of biogenic calcite and authigenic overgrowth geochemistry**

456 SIMS spot analyses ( $\sim 10$   $\mu\text{m}$  diameter) are similar to the *G. ruber* (w) test wall thickness ( $\sim 9$ –  
457  $12$   $\mu\text{m}$ ) such that a large proportion of the measurements partly overlapped onto epoxy. The  
458 location of these compromised analyses ( $n = 35$ ) was confirmed by SEM observation, and  
459 only those measurements which were located solely on the foraminifera test were included in  
460 the reported analyses (Fig. 7, Supplementary Material 3). Overall, 16 SIMS and 36 EPMA  
461 spot measurements from the F-0 (final), F-1 (penultimate) and F-2 (antepenultimate)  
462 chambers were measured on seven samples for *G. ruber* (w), (Fig. 7, Supplementary  
463 Materials 2-3). An additional five EPMA spot analyses of large authigenic overgrowths were  
464 measured (Fig. 7, Supplementary Material 2). Limited SIMS and EPMA sample sets were  
465 obtained due to the limitations of spot size (for SIMS) and epoxy stability (for EPMA). Yet,  
466 the datasets are still deemed sufficient to assess overall trends and the application of these  
467 micro-analytical techniques in foraminiferal diagenetic studies. Mean values and standard  
468 deviations of the measurements along with sample locations (with reference on the  $\delta^{18}\text{O}$  *G.*  
469 *ruber* (w) curve) are shown in Figure 7.

470

471 **Fig. 7. (a) SIMS and (b) EPMA spot data versus whole-test ICP-MS/ICP-OES**  
472 **measurements for *G. ruber* (w) with the location of the samples (circles with number ID:**  
473 **black = SIMS and red = EPMA samples) referenced on (c) the long-term *G. ruber* (w)**

474  $\delta^{18}\text{O}$  curve; (d) *G. ruber* (w) whole-test Mg/Ca data and (e) the *G. ruber* (w) Diagenesis  
475 Rank (DR) color map. IODP Expedition 359 Site U1467 sample IDs: (1) A, B-Mudline;  
476 (2) B-3H-3, 9-10 cm; (3) B-4H-5, 36-37 cm; (4) B-6H-2, 75-76 cm; (5) B-6H-3, 75-76 cm;  
477 (6) B-6H-4, 75-76 cm; (7) B-7H-3, 75-76 cm. Sea surface temperature (SST) calculations  
478 are based on the *G. ruber* (w) equation of Anand et al. (2003). Red curve shows  $\delta^{18}\text{O}$  *G.*  
479 *ruber* (w) data from Bunzel et al. (2017). A 3-pt moving average smoothing was applied  
480 to all datasets (thick lines) to highlight the cycles. Note: F-0 (final), F-1 (penultimate)  
481 and F-2 (antepenultimate) chambers, WT= whole-test and OG = overgrowth  
482 measurements. WT data in a) and b) for A, B-Mudline Sample 1 is from Stainbank et al.  
483 (2019).

484

485 Whole-test  $\delta^{18}\text{O}$  and Mg/Ca values are comparable to SIMS and EPMA spot measurements  
486 for core-top Sample 1 at 0 ka (0 mcd) and to EPMA data for Sample 2 at 409.0 ka (17.4 mcd).  
487 From Sample 3 (= 864.7 ka, 31.3 mcd) to Sample 7 (= 1743.8 ka, 58.7 mcd) the whole-test *G.*  
488 *ruber* geochemical values are consistently higher than the SIMS ( $z = 1.5\text{-}5.2$ ;  $p = 0.9\text{-}1$ ) and  
489 EPMA ( $z = 2.7\text{-}8$ ;  $p = 1$ ) data obtained from individual chambers (Fig. 7a-b). Moreover, the  
490 difference varies with the highest values and largest offsets in the deepest, oldest sample.  
491 Interestingly, one F-1 SIMS data point for Sample 7 hit substantial diagenetic overgrowths  
492 and has a relatively high  $\delta^{18}\text{O}$  value of  $-1.24\text{‰}$  (Supplementary Material 3). The EPMA  
493 overgrowth data (Samples 6 and 7) reveals a HMC composition with 3–6 times higher Mg/Ca  
494 values than original test compositions. Samples 3–7 cover the interval corresponding to an  
495 observed change in the slope of the long-term *G. ruber* (w)  $\delta^{18}\text{O}$  record with a down-core  
496 trend towards higher values. A marked increase in the slope of the long-term *G. ruber* (w)  
497 Mg/Ca record is, however, already noted prior to Sample 3 (Fig. 7d). Similar to the EPMA  
498 spot analyses (Fig. 7b), the elemental maps of both *G. ruber* (w) and *P. obliquiloculata* (w/c)

499 show clear Mg enrichment in the authigenic overgrowths (Fig. 8). Both species have a LMC  
500 test (Figs. 8.a1, 8.b1), whereas *P. obliquiloculata* (w/c) has natural HMC growth bands  
501 indicated on Figure 8 (yellow arrows). Overgrowths, on both the inner and outer test surfaces,  
502 have 4–10 times higher Mg intensities than the biogenic calcite (Figs. 8.a2, 8.b2).

503

504 **Fig. 8. Mg (intensity) EPMA maps. Examples of IODP Expedition 359 Hole U1467B**  
505 **pristine specimens (Mudline) are shown for (a1) *G. ruber* (w) and (b1) *P. obliquiloculata***  
506 **(w/c) with diagenetically altered examples shown for (a2) *G. ruber* (w) (7H-3, 75-76 cm)**  
507 **and (b2) *P. obliquiloculata* (w/c) (6H-4, 75-76 cm). T = test, OG = overgrowth, EE = edge**  
508 **effect. Reference to sample locations (ID1, 6 and 7) are shown on Fig. 7. Note the high-**  
509 **Mg (yellow arrows) and low-Mg banding in the *P. obliquiloculata* (w/c) tests. Scale bars**  
510 **= 10  $\mu\text{m}$ .**

511

## 512 4. DISCUSSION

### 513 4.1. Preservation state of the individual long-term geochemical records

514 The stable oxygen isotope composition ( $\delta^{18}\text{O}$ ) of the original foraminiferal test is a function of  
515 the ambient seawater temperature and  $\delta^{18}\text{O}$  composition during its initial precipitation  
516 (Pearson, 2012). Similarly, biogenic test Mg/Ca ratios reflect ambient seawater temperatures  
517 (e.g. Raddatz et al., 2017; Rippert et al., 2016). Authigenic overgrowth is anticipated to occur  
518 near the sediment/bottom-water interface and down-core (e.g. Regenberget al., 2007). As  
519 such, its oxygen isotope composition is controlled by a variety of factors including  
520 thermodynamic fractionation, the  $\delta^{18}\text{O}$  and pH of the precipitating fluid as well as mineralogy  
521 and kinetic effects during the precipitation (Kim and O'Neil, 1997; O'Neil et al., 1969; Swart,  
522 2015). The elemental ratio compositions are related to site mineralogy and pore water  
523 geochemistry.

524

525 From 0 to ~200 kyr (0 to ~7.3 mcd), the cycles and amplitudes of IODP Expedition 359 Site  
526 U1467  $\delta^{18}\text{O}$  *G. ruber* (w) and *C. mabahethi* records, are comparable to the records produced  
527 by Bunzel et al. (2017) (Fig. 6). Bunzel et al. (2017) compiled stable isotopic datasets from  
528 Core SO236-052-4 retrieved from the Maldives Inner Sea (03°55.09'N; 73°08.48'E) at a water  
529 depth of 382 m (Note: the slight amplitudinal difference between the benthic datasets is due to  
530 differences in study site depths). Notably, Bunzel et al. (2017) used a lower analytical  
531 resolution and a larger test size (250–350  $\mu\text{m}$ ) for their *G. ruber* (w) record, yet visually the  
532 two datasets are nearly identical. This attests to the good preservation state of Site U1467  
533 samples for the first ~200 kyr (7.3 mcd). Furthermore, we can consider the *G. ruber* (w)  $\delta^{18}\text{O}$   
534 and Mg/Ca records from 0 to ~627.4 kyr (0 to ~24.7 mcd) to be pristine/near-pristine. This is  
535 reflected by the low DR values (0-2) and is manifest in the coherence between the SIMS and  
536 EPMA spot analyses data (Samples 1 and 2) and the whole-test geochemical datasets. In  
537 particular, EPMA data for Sample 2 (Fig. 7b) illustrates that at least up until 409.0 ka (17.4  
538 mcd) the whole-test Mg/Ca values closely reflect the original test geochemistry. While small,  
539 patchy HMC overgrowth is present on the internal surfaces (DR = 1), it does not appear to be  
540 sufficient to bias the whole-test geochemistry. Calculated SSTs are also notable for being  
541 within the modern, seasonal seawater temperature range (Fig. 7d) (Krahmann and Krüger,  
542 2018; Quadfasel, 2017; Reolid et al., 2017).

543

544 The degree of influence of the authigenic overgrowth on whole-test geochemical records can  
545 vary significantly and is not necessarily consistent across the various proxies (i.e.  $\delta^{18}\text{O}$  versus  
546 Mg/Ca). A change in the preservation state of the *G. ruber* (w) tests occurs between ~627.4 to  
547 790.0 kyr (24.7–28.7 mcd) onwards (DR values > 2). Discrepancies are also recorded by the  
548 SIMS and EPMA data from individual chambers which are significantly lower than respective

549 whole-test geochemical values from Sample 3 ( $\Delta \sim 1.1$  ‰ and  $\sim 1.5$  mmol/mol, respectively) to  
550 Sample 7 ( $\Delta \sim 1.8$  ‰ and  $\sim 4.1$  mmol/mol, respectively) (Fig. 7a, b). There is a notable down-  
551 core increase in the slope of the  $\delta^{18}\text{O}$  *G. ruber* (w) record. This is captured by SIMS Samples  
552 3–5, which show a  $\sim 1$  ‰ increase in the whole-test values and Sample 7, the most  
553 diagenetically altered, which shows a  $\sim 2$  ‰ increase. The compositional trends observed in  
554 the  $\delta^{18}\text{O}$  data are notably amplified in the long-term Mg/Ca record, with a steeper down-core  
555 slope increase. Considering the original test geochemistry is usually  $< 6$  mmol/mol, only a  
556 limited amount of HMC overgrowth ( $\sim 12$ – $22$  mmol/mol) would be required to bias the  
557 whole-test Mg/Ca towards significantly higher values (Fig. 7). This is reflected in EPMA  
558 Sample 3 (= 864.7 ka, 31.3 mcd), which has minimal overgrowth present on the external test  
559 surface (external category Diagenesis Rank = 1), yet small-medium well-developed euhedral  
560 crystals across the entire inner test surface (internal category Diagenesis Rank = 2). This  
561 overgrowth, although small, is sufficient to elevate the whole-test Mg/Ca values and increase  
562 the SST reconstruction by  $\sim 2^\circ\text{C}$ . This is further substantiated by EPMA Samples 4, 6 and 7,  
563 which have higher DR values due to poorer preservation states and an increased presence  
564 and/or size of overgrowth crystals. All have lower spot F-0 and F-1 chamber Mg/Ca values in  
565 comparison to the whole-test data, resulting in progressively larger discrepancies in SST  
566 estimates of  $\sim 4$ – $7^\circ\text{C}$ .

567

568 The precipitation of HMC overgrowths, as opposed to the more stable LMC, could be a  
569 function of both the composition and content of the bulk sediment as well as the pore water  
570 geochemistry (e.g. Panieri et al., 2017; Regenberg et al., 2007). At Site U1467, HMC is only  
571 present in the top 10 mbsf (Fig. 2). Where HMC in the sediment has dissolved,  $\text{Mg}^{2+}$  is  
572 released and may be incorporated (elsewhere) in crystalline overgrowths on biogenic  
573 carbonates. Aragonite dissolution and active sulphate reduction were noted below 50 mbsf at



574 this site by Betzler et al. (2017). The former had been noted earlier in a pteropod study by  
575 Sreevidya et al. (2019) who reported intense dissolution of aragonitic pteropods beyond ~800  
576 ka. As such, an increased saturation state of pore waters, with respect to  $Mg^{2+}$ , in combination  
577 with active sulphate reduction may have favored HMC over LMC authigenic precipitates  
578 (Panieri et al., 2017; Swart, 2015). Higher resolution sediment mineralogy together with  
579 petrography and pore water profiles are needed to conclude as to the exact processes behind  
580 the depth occurrence and Mg-content of the HMC overgrowths. However, the combined  
581 influence of HMC with naturally elevated  $\delta^{18}O$  values (Tarutani et al., 1969), with  
582 thermodynamic fraction ( $\Delta \sim 19^\circ C$  between the surface seawater and at 487 m depth) and  
583 related fluid geochemistry changes would further justify the precipitation of authigenic  
584 overgrowths with elevated  $\delta^{18}O$  values. These processes could thus explain the notable biases  
585 (stable isotopic and elemental) on the planktonic whole-test geochemical data from  
586 SIMS/EPMA Sample 3 (= 864.7 ka, 31.3 mcd) to 7 (= 1743.8 ka, 58.7 mcd).

587

588 Although no SIMS or EPMA data was collected for the benthic *C. mabahethi* species, a  
589 change in preservation state ( $DR > 2$ ) occurs between ~790.0 to 807.9 kyr (28.7–29.1 mcd).  
590 As such, we can surmise the records beyond this interval to have some degree of diagenetic  
591 overprint (Figs. 6e-f). This is supported by observations of large, well-developed overgrowth  
592 on the internal test surfaces at 872.0 ka (31.7 mcd). Even though minimal overgrowth is  
593 present on the external surfaces, it is presumed that the large internal crystals would be  
594 sufficient to affect the whole-test geochemical records. However, although the Mg/Ca biases  
595 would be similar to that on the *G. ruber* (w) records, the  $\delta^{18}O$  influences should be minor  
596 considering diagenetic precipitation is anticipated to occur near the sediment/bottom water  
597 interface in close proximity to where the original biogenic calcite precipitated (Edgar et al.,  
598 2013). This would imply similar seawater temperatures; however, differences in pH,

599 mineralogy and kinetic effects during the authigenic overgrowth precipitation cannot be  
600 excluded. This hypothesis is supported by the prominent glacial-interglacial cycles with their  
601 amplitudes seemingly well preserved for the entirety of the benthic  $\delta^{18}\text{O}$  record (0-1179.0 kyr)  
602 (Figs. 3-4, 6).

603

#### 604 **4.2. Diagenetic susceptibility of individual planktonic species**

605 We found distinct differences in the preservation state of the three investigated planktonic  
606 species. As such, the diagenetic bias on their respective whole-test geochemical compositions  
607 varies. This is illustrated in Intervals 1-3 in Figure 6, with a variable preservation of the  
608 glacial-interglacial amplitudinal differences. The whole-test *G. ruber* (w), *G. glutinata* (w/b)  
609 and *P. obliquiloculata* (w/c)  $\delta^{18}\text{O}$  records all reflect clear, large amplitude cycles within  
610 Interval 1. However, relative to the thicker-walled *P. obliquiloculata* (w/c), the former two  
611 species record dampened signals with the peaks notably less pronounced across Interval 2.  
612 Across Interval 3, in the most diagenetically altered portion of the record, all datasets are  
613 notably affected with reduced glacial-interglacial maxima and minima and all  $\delta^{18}\text{O}$  records  
614 converge because of increasing whole test  $\delta^{18}\text{O}$  values.

615

616 It might seem contradictory that the species, which appears to be most diagenetically  
617 susceptible, would have the best whole-test geochemical preservation across Interval 2.  
618 However, as *P. obliquiloculata* (w/c) has the thickest test (~24  $\mu\text{m}$ , Figs. 5, 9), the rationale is  
619 that a thicker test would equate to more of the whole-test composition being weighted by the  
620 biogenic calcite. Therefore, in proportion to the primary signal, the authigenic overgrowth  
621 would contribute a smaller percentage and result in a smaller bias compared to *G. ruber* (w)  
622 and *G. glutinata* (w/b) which have significantly thinner tests (~9–12 and ~6–10  $\mu\text{m}$ ,  
623 respectively; Figs. 5, 9). This is in accordance with observations by Bé (1977) and Kucera

624 (2007). Bé (1977) correlated increased diagenetic resistance for species with smaller pores,  
625 thicker walls and larger test size, while Kucera (2007) reports an increase in dissolution  
626 resistance for species with a lower porosity (Fig. 9).

627

628 **Fig. 9. Interpretations of diagenetic susceptibilities for the whole-test geochemistry of the**  
629 **three investigated planktonic species. Interpretations are based on Diagenesis Rank**  
630 **(DR) values, spot EPMA/SIMS and whole-test geochemistry data from IODP Expedition**  
631 **359 Site U1467. Interpretations of dissolution susceptibilities after Kucera (2007).**

632

## 633 5. CONCLUSIONS

634 Foraminiferal geochemical records from shallow, carbonate platforms are integral for  
635 understanding global paleoceanographic and -climatic trends but are subject to diagenetic  
636 influences. This is the case at IODP Expedition 359 Site U1467, which represents a shallow-  
637 intermediate water archive from the equatorial Indian Ocean of importance for South Asian  
638 Monsoon (SAM) climatic studies and latitudinal scale shifts of ocean currents. Prior to  
639 utilizing our high-analytically resolved geochemical records for paleo-reconstructions, it is  
640 important to constrain the influence of diagenetic alteration on both the preservation of the  
641 original geochemical compositions and long-term cyclicality.

642

643 The presence and influence of authigenic overgrowths on the inside and/or outside of the  
644 foraminiferal test as well as through the partial or full recrystallization of the test wall has  
645 long been recognised. Importantly, this authigenic calcite is not ubiquitous or uniform in  
646 terms of presence, size, distribution or geochemical composition and as such should be  
647 assessed on an individual study site basis. For simplicity, ease of use and to facilitate  
648 reproducibility in other studies, the qualitative DR detailed and used in this study only

649 constrains the presence of authigenic overgrowths on the test surfaces as well as within the  
650 wall structure. However, it is noted that both the primary and authigenic calcite can be  
651 susceptible to dissolution, which would further alter the geochemical compositions. These  
652 dissolution features, which can include etched surfaces as well as lattice-like calcite  
653 structures, as well as partial recrystallization of the wall texture are noted in the deepest,  
654 oldest studied samples.

655

656 The degree of influence of the authigenic overgrowth on the whole-test geochemistry varies  
657 across the foraminiferal species (*G. ruber* (w), *G. glutinata* (w/b), *P. obliquiloculata* (w/c), *C.*  
658 *mabahethi*) and proxies (i.e.  $\delta^{18}\text{O}$  versus Mg/Ca). Considering the site mineralogy, whole-test  
659 Mg/Ca compositions are notably more impacted than  $\delta^{18}\text{O}$  records. However, taking into  
660 consideration our individual spot analyses (SIMS and EPMA) and DR data, the top ~627.4  
661 kyr of the *G. ruber* (w) Mg/Ca and  $\delta^{18}\text{O}$  records are well preserved and largely reflect the  
662 primary geochemical compositions. Given the setting of overgrowth precipitation, the benthic  
663 *C. mabahethi*  $\delta^{18}\text{O}$  record from 0–790.0 kyr (DR = 0–2), if not the entire benthic record, is  
664 considered to have pristine/near-pristine preservation of the primary  $\delta^{18}\text{O}$  signal. As such, the  
665 top portions of both the *G. ruber* (w) (0 to ~627.4 kyr; 0–24.7 mcd) and *C. mabahethi* (0 to  
666 ~790.0 kyr; 0–28.7 mcd) records (whole-test data) are suitable for paleoceanographic  
667 reconstructions of absolute seawater temperature, salinity and  $\delta^{18}\text{O}$  values. Notwithstanding  
668 the down-core diagenetic influences, the glacial-interglacial cyclicity, while dampened, is  
669 maintained as attested by the coherence of both the *G. ruber* (w) and *C. mabahethi*  $\delta^{18}\text{O}$   
670 records with Prob-stack. As such, the complete geochemical records could still be used for  
671 cyclostratigraphy to assess long-term orbital scale properties.

672

673 Overall, we show foraminiferal species (e.g. *P. obliquiloculata*) with thicker tests are better  
674 suited for whole-test geochemical analyses, in diagenetically susceptible settings, as they have  
675 a higher proportion of biogenic calcite relative to authigenic overgrowth. Moreover, while  
676 only a portion of our whole-test geochemical records reflect the primary compositions, SIMS  
677 and EPMA spot measurements can be utilized to overcome any biases in diagenetically  
678 impacted intervals. Considering the importance of these types of records for tropical  
679 temperature studies, it is vital to employ an approach, whether it be spot versus whole-test  
680 analyses, the utilization of specimens with thicker tests or a visual DR, which will allow the  
681 preservation state to be assessed to obtain more accurate and reliable paleo-reconstructions.

682

## 683 **6. ACKNOWLEDGEMENTS**

684 Funding: This work was funded by the Swiss National Science Foundation (SNSF) through  
685 grant number 200021\_165852/1 awarded to SSp. DK acknowledges funding support from the  
686 Natural Environment Research Council (NERC) through grant number NERC-  
687 NE/N012739/1. Additionally, EDB was funded through the SNSF project  
688 QuantiCarb@Spring (project number: 154810).

689

690 The authors would like to thank the International Ocean Discovery Program (IODP) for  
691 supplying the samples used in this study. From the University of Fribourg, we thank Alex  
692 Salzmann for his help with embedding the EPMA and SIMS samples, Christoph Neururer for  
693 his help with the SEM imaging and Sandra Borderie for her help with Figure 1, which was  
694 drawn using the free software package GMT (The Generic Mapping Tools; Wessel and  
695 Smith, 1991). Martin Robyr is thanked for his assistance during the EPMA analysis at the  
696 University of Lausanne. FIERCE is financially supported by the Wilhelm and Else Heraeus  
697 Foundation, which is gratefully acknowledged. This is FIERCE contribution No. 19. Lastly,

698 we acknowledge the constructive comments of two anonymous reviewers that helped to refine  
699 the manuscript.

700

## 701 REFERENCES

702 Ahn, S., Khider, D., Lisiecki, L.E., Lawrence, C.E., 2017. A probabilistic Pliocene–  
703 Pleistocene stack of benthic  $\delta^{18}\text{O}$  using a profile hidden Markov model. *Dyn. Stat. Clim.*  
704 *Syst.* 2, 1–16. <https://doi.org/10.1093/climsys/dzx002>

705 Anand, P., Elderfield, H., Conte, M.H., 2003. Calibration of Mg/Ca thermometry in  
706 planktonic foraminifera from a sediment trap time series. *Paleoceanography* 18, 1050.  
707 <https://doi.org/10.1029/2002PA000846>

708 Barker, S., Greaves, M., Elderfield, H., 2003. A study of cleaning procedures used for  
709 foraminiferal Mg/Ca paleothermometry. *Geochemistry, Geophys. Geosystems* 4, 8407.  
710 <https://doi.org/10.1029/2003GC000559>

711 Bé, A.W.H., 1977. An ecological, zoogeographic and taxonomic review of recent planktonic  
712 foraminifera. *Ocean. Micropaleontol.* 1, 1–100.

713 Bé, A.W.H., 1968. Shell porosity of Recent planktonic foraminifera as a climatic index.  
714 *Science* (80-. ). 161, 881–884.

715 Betzler, C., Eberli, G.P., Alvarez Zarikian, C.A., Alonso-García, M., Bialik, O.M., Blättler,  
716 C.L., Guo, J.A., Haffen, S., Horozal, S., Inoue, M., Jovane, L., Kroon, D., Lanci, L.,  
717 Laya, J.C., Ling Hui Mee, A., Lüdmann, T., Nakakuni, M., Nath, B.N., Niino, K.,  
718 Petruny, L.M., Pratiwi, S.D., Reijmer, J.J.G., Reolid, J., Slagle, A.L., Sloss, C.R., Su, X.,  
719 Swart, P.K., Wright, J.D., Yao, Z., Young, J.R., 2017. Proceedings of the International  
720 Ocean Discovery Program Volume, 359. Coll. Station. TX (International Ocean Discov.  
721 Program). <https://doi.org/10.14379/iodp.proc.359.102.2017>

722 Betzler, C., Eberli, G.P., Kroon, D., Wright, J.D., Swart, P.K., Nath, B.N., Alvarez-Zarikian,

723 C.A., Alonso-García, M., Bialik, O.M., Blättler, C.L., Guo, J.A., Haffen, S., Horozal, S.,  
724 Inoue, M., Jovane, L., Lanci, L., Laya, J.C., Ling Hui Mee, A., Lüdmann, T., Nakakuni,  
725 M., Niino, K., Petruny, L.M., Pratiwi, S.D., Reijmer, J.J.G., Reolid, J., Slagle, A.L.,  
726 Sloss, C.R., Su, X., Yao, Z., Young, J.R., 2016. The abrupt onset of the modern South  
727 Asian Monsoon winds. *Sci. Rep.* 6, 29838. <https://doi.org/10.1038/srep29838>

728 Betzler, C., Eberli, G.P., Lüdmann, T., Reolid, J., Kroon, D., Reijmer, J.J.G., Swart, P.K.,  
729 Wright, J., Young, J.R., Alvarez-Zarikian, C., Alonso-García, M., Bialik, O.M., Blättler,  
730 C.L., Guo, J.A., Haffen, S., Horozal, S., Inoue, M., Jovane, L., Lanci, L., Laya, J.C., Hui  
731 Mee, A.L., Nakakuni, M., Nath, B.N., Niino, K., Petruny, L.M., Pratiwi, S.D., Slagle,  
732 A.L., Sloss, C.R., Su, X., Yao, Z., 2018. Refinement of Miocene sea level and monsoon  
733 events from the sedimentary archive of the Maldives (Indian Ocean). *Prog. Earth Planet.*  
734 *Sci.* 5, 5. <https://doi.org/10.1186/s40645-018-0165-x>

735 Birch, H., Coxall, H.K., Pearson, P.N., Kroon, D., O'Regan, M., 2013. Planktonic  
736 foraminifera stable isotopes and water column structure: Disentangling ecological  
737 signals. *Mar. Micropaleontol.* 101, 127–145.  
738 <https://doi.org/doi.org/10.1016/j.marmicro.2013.02.002>

739 Blättler, C.L., Higgins, J.A., Swart, P.K., 2019. Advected glacial seawater preserved in the  
740 subsurface of the Maldives carbonate edifice. *Geochim. Cosmochim. Acta* 257, 80–95.  
741 <https://doi.org/doi.org/10.1016/j.gca.2019.04.030>

742 Bunzel, D., Schmiedl, G., Lindhorst, S., Mackensen, A., Reolid, J., Romahn, S., Betzler, C.,  
743 2017. A multi-proxy analysis of Late Quaternary ocean and climate variability for the  
744 Maldives, Inner Sea. *Clim. Past* 13, 1791–1813. [https://doi.org/10.5194/cp-13-1791-](https://doi.org/10.5194/cp-13-1791-2017)  
745 2017

746 Detlef, H., Sosdian, S.M., Kender, S., Lear, C.H., Hall, I.R., 2020. Multi-elemental  
747 composition of authigenic carbonates in benthic foraminifera from the eastern Bering

748 Sea continental margin (International Ocean Discovery Program Site U1343 ). *Geochim.*  
749 *Cosmochim. Acta* 268, 1–21. <https://doi.org/10.1016/j.gca.2019.09.025>

750 Edgar, K.M., Anagnostou, E., Pearson, P.N., Foster, G.L., 2015. Assessing the impact of  
751 diagenesis on  $\delta^{11}\text{B}$ ,  $\delta^{13}\text{C}$ ,  $\delta^{18}\text{O}$ , Sr/Ca and B/Ca values in fossil planktic foraminiferal  
752 calcite. *Geochim. Cosmochim. Acta* 166, 189–209.  
753 <https://doi.org/10.1016/j.gca.2015.06.018>

754 Edgar, K.M., Pälike, H., Wilson, P.A., 2013. Testing the impact of diagenesis on the  $\delta^{18}\text{O}$  and  
755  $\delta^{13}\text{C}$  of benthic foraminiferal calcite from a sediment burial depth transect in the  
756 equatorial Pacific. *Paleoceanography* 28, 468–480. <https://doi.org/10.1002/palo.20045>

757 Elderfield, H., Yu, J., Anand, P., Kiefer, T., Nyland, B., 2006. Calibrations for benthic  
758 foraminiferal Mg/Ca paleothermometry and the carbonate ion hypothesis. *Earth Planet.*  
759 *Sci. Lett.* 250, 633–649. <https://doi.org/doi:10.1016/j.epsl.2006.07.041>

760 GEBCO Compilation Group. 2019. GEBCO 2019 Grid. [http://doi:10.5285/836f016a-33be-](http://doi:10.5285/836f016a-33be-6ddc-e053-6c86abc0788e)  
761 [6ddc-e053-6c86abc0788e](http://doi:10.5285/836f016a-33be-6ddc-e053-6c86abc0788e)

762 Groeneveld, J., Nürnberg, D., Tiedemann, R., Reichert, G.J., Steph, S., Reuning, L., Crudeli,  
763 D., Mason, P., 2008. Foraminiferal Mg/Ca increase in the Caribbean during the Pliocene:  
764 Western Atlantic Warm Pool formation, salinity influence, or diagenetic overprint?  
765 *Geochemistry, Geophys. Geosystems* 9, Q01P23.  
766 <https://doi.org/10.1029/2006GC001564>

767 Gupta, A.K., Sarkar, S., De, S., Clemens, S.C., Velu, A., 2010. Mid-Brunhes strengthening of  
768 the Indian Ocean Dipole caused increased equatorial East African and decreased  
769 Australasian rainfall. *Geophys. Res. Lett.* 37, L06706.  
770 <https://doi.org/10.1029/2009GL042225>

771 Hastenrath, S., Nicklis, A., Greischar, L., 1993. Atmospheric-Hydrospheric mechanisms of  
772 climate anomalies in the western equatorial Indian Ocean. *J. Geophys. Res.* 98, 20,219-



773 20,235. <https://doi.org/10.1029/2004JD004981>

774 Kim, S.-T., O'Neil, J.R., 1997. Equilibrium and nonequilibrium oxygen isotope effects in  
775 synthetic carbonates. *Geochim. Cosmochim. Acta* 61, 3461–3475.  
776 [https://doi.org/10.1016/S0016-7037\(97\)00169-5](https://doi.org/10.1016/S0016-7037(97)00169-5)

777 Krahmann, G., Krüger, K., 2018. Physical oceanography during SONNE cruise SO235.  
778 PANGAEA. <https://doi.org/10.1594/PANGAEA.887805>

779 Kroon, D., Ganssen, G., 1989. Northern Indian Ocean upwelling cells and the stable isotope  
780 composition of living planktonic foraminifers. *Deep Sea Res.* 36, 1219–1236.  
781 [https://doi.org/10.1016/0198-0149\(89\)90102-7](https://doi.org/10.1016/0198-0149(89)90102-7)

782 Kucera, M., 2007. Chapter Six planktonic foraminifera as tracers of past oceanic  
783 environments, in: *Developments in Marine Geology*. pp. 213–262.  
784 [https://doi.org/10.1016/S1572-5480\(07\)01011-1](https://doi.org/10.1016/S1572-5480(07)01011-1)

785 Kunkelova, T., Jung, S.J.A., de Leau, E.S., Odling, N., Thomas, A.L., Betzler, C., Eberli,  
786 G.P., Alvarez-Zarikian, C.A., Alonso-García, M., Bialik, O.M., Blättler, C.L., Guo, J.A.,  
787 Haffen, S., Horozal, S., Ling Hui Mee, A., Inoue, M., Jovane, L., Lanci, L., Laya, J.C.,  
788 Lüdmann, T., Bejugam, N.N., Nakakuni, M., Niino, K., Petruny, L.M., Pratiwi, S.D.,  
789 Reijmer, J.J.G., Reolid, J., Slagle, A.L., Sloss, C.R., Su, X., Swart, P.K., Wright, J.D.,  
790 Yao, Z., Young, J.R., Lindhorst, S., Stainbank, S., Rueggeberg, A., Spezzaferri, S.,  
791 Carrasqueira, I., Yu, S., Kroon, D., 2018. A two million year record of low-latitude  
792 aridity linked to continental weathering from the Maldives. *Prog. Earth Planet. Sci.* 5, 86.  
793 <https://doi.org/10.1186/s40645-018-0238-x>

794 Lisiecki, L.E., Raymo, M.E., 2005. A Pliocene-Pleistocene stack of 57 globally distributed  
795 benthic  $\delta^{18}\text{O}$  records. *Paleoceanography* 20, PA1003.  
796 <https://doi.org/10.1029/2004PA001071>

797 Lüdmann, T., Kalvelage, C., Betzler, C., Fürstenau, J., Hübscher, C., 2013. The Maldives, a

798 giant isolated carbonate platform dominated by bottom currents. *Mar. Pet. Geol.* 43.  
799 <https://doi.org/10.1016/j.marpetgeo.2013.01.004>

800 O’Neil, J.R., Clayton, R.N., Mayeda, T.K., 1969. Oxygen isotope fractionation in divalent  
801 metal carbonates. *J. Chem. Phys.* 51, 5547–5558. <https://doi.org/10.1063/1.1671982>

802 Paillard, D., Labeyrie, L., Yiou, P., 1996. Macintosh program performs time-series analysis.  
803 *Eos (Washington, DC)*. 77, 379. <https://doi.org/10.1029/96eo00259>

804 Panieri, G., Lepland, A., Whitehouse, M.J., Wirth, R., Raanes, M.P., James, R.H., Graves,  
805 C.A., Crémère, A., Schneider, A., 2017. Diagenetic Mg-calcite overgrowths on  
806 foraminiferal tests in the vicinity of methane seeps. *Earth Planet. Sci. Lett.* 458, 203–212.  
807 <https://doi.org/10.1016/j.epsl.2016.10.024>

808 Pearson, P.N., 2012. Oxygen isotopes in foraminifera: Overview and historical review, in:  
809 Ivany, L.C., Huber, B.T. (Eds.), *Reconstructing Earth’s Deep-Time Climate-The State of*  
810 *the Art in 2012*, Paleontological Society Short Course, November 3. The Paleontological  
811 Society Papers, pp. 1–38.

812 Quadfasel, D., 2017. Physical oceanography during RV SONNE cruise SO127, 17 December  
813 1997 to 7 January 1998 from Port Klang to Malé. *PANGAEA*.  
814 <https://doi.org/10.1594/PANGAEA.881513>

815 Raddatz, J., Nürnberg, D., Tiedemann, R., Rippert, N., 2017. Southeastern marginal West  
816 Pacific Warm Pool sea-surface and thermocline dynamics during the Pleistocene (2.5–  
817 0.5 Ma). *Palaeogeogr. Palaeoclimatol. Palaeoecol.* 471, 144–156.  
818 <https://doi.org/10.1016/j.palaeo.2017.01.024>

819 Rebotim, A., Voelker, A.H.L., Jonkers, L., Waniek, J.J., Meggers, H., Schiebel, R., Fraile, I.,  
820 Schulz, M., Kucera, M., 2017. Factors controlling the depth habitat of planktonic  
821 foraminifera in the subtropical eastern North Atlantic. *Biogeosciences* 14, 827–859.  
822 <https://doi.org/10.5194/bg-14-827-2017>

823 Regenberg, M., Nürnberg, D., Schönfeld, J., Reichart, G.-J., 2007. Early diagenetic overprint  
824 in Caribbean sediment cores and its effect on the geochemical composition of planktonic  
825 foraminifera. *Biogeosciences* 4, 957–973. <https://doi.org/10.5194/bg-4-957-2007>

826 Reolid, J., Reolid, M., Betzler, C., Lindhorst, S., Wiesner, M.G., Lahajnar, N., 2017. Upper  
827 Pleistocene cold-water corals from the Inner Sea of the Maldives: taphonomy and  
828 environment. *Facies* 63, 8. <https://doi.org/10.1007/s10347-016-0491-7>

829 Rippert, N., Nürnberg, D., Raddatz, J., Maier, E., Hathorne, E., Bijma, J., Tiedemann, R.,  
830 2016. Constraining foraminiferal calcification depths in the western Pacific warm pool.  
831 *Mar. Micropaleontol.* 128, 14–27. <https://doi.org/10.1016/j.marmicro.2016.08.004>

832 Sadekov, A.Y., Ganeshram, R., Pichevin, L., Berdin, R., McClymont, E., Elderfield, H.,  
833 Tudhope, A.W., 2013. Palaeoclimate reconstructions reveal a strong link between El  
834 Niño-Southern Oscillation and Tropical Pacific mean state. *Nat. Commun.* 4, 2692.  
835 <https://doi.org/10.1038/ncomms3692>

836 Schott, F.A., Xie, S.-P., McCreary Jr, J.P., 2009. Indian Ocean circulation and climate  
837 variability. *Rev. Geophys.* 47, RG1002. <https://doi.org/10.1029/2007RG000245>

838 Sreevidya, E., Sijinkumar, A.V., Nath, B.N., 2019. Aragonite pteropod abundance and  
839 preservation records from the Maldives, equatorial Indian Ocean: Inferences on past  
840 oceanic carbonate saturation and dissolution events. *Palaeogeogr. Palaeoclimatol.*  
841 *Palaeoecol.* 534, 109313. <https://doi.org/10.1016/j.palaeo.2019.109313>

842 Stainbank, S., Kroon, D., Rüggeberg, A., Raddatz, J., de Leau, E.S., Zhang, M., Spezzaferri,  
843 S., 2019. Controls on planktonic foraminifera apparent calcification depths for the  
844 northern equatorial Indian Ocean. *PLoS One* 14, e0222299.  
845 <https://doi.org/10.1371/journal.pone.0222299>

846 Steinhardt, J., Cléroux, C., De Nooijer, L.J., Brummer, G.-J., Zahn, R., Ganssen, G., Reichart,  
847 G.-J., 2015. Reconciling single-chamber Mg/Ca with whole-shell  $\delta^{18}\text{O}$  in surface to

848 deep-dwelling planktonic foraminifera from the Mozambique Channel. *Biogeosciences*  
849 12, 2411–2429. <https://doi.org/10.5194/bg-12-2411-2015>

850 Swart, P.K., 2015. The geochemistry of carbonate diagenesis: The past, present and future.  
851 *Sedimentology* 62, 1233–1304. <https://doi.org/10.1111/sed.12205>

852 Tarutani, T., Clayton, R.N., Mayeda, T.K., 1969. The effect of polymorphism and magnesium  
853 substitution on oxygen isotope fractionation between calcium carbonate and water.  
854 *Geochim. Cosmochim. Acta* 33, 987–996. [https://doi.org/10.1016/0016-7037\(69\)90108-](https://doi.org/10.1016/0016-7037(69)90108-2)  
855 2

856 Wessel, P., Smith, W.H., 1991. Free software helps map and display data. *Eos. Trans. AGU*  
857 72 (41), 441–446.

858  
859  
860  
861  
862  
863  
864  
865  
866  
867  
868  
869  
870  
871  
872

873 **Supplementary Material 1. Representative visual SEM images used to define the**  
874 **Diagenesis Rank (DR) values for the individual species from IODP Expedition 359 Site**  
875 **U1467.**

876

877 **Supplementary Material 2. Electron Probe Micro-Analyzer (EPMA) data.**

878

879 **Supplementary Material 3. Secondary Ion Mass Spectrometer (SIMS) data.**

880

881 **Supplementary Material 4. Age model data for IODP Expedition 359 Site U1467.**

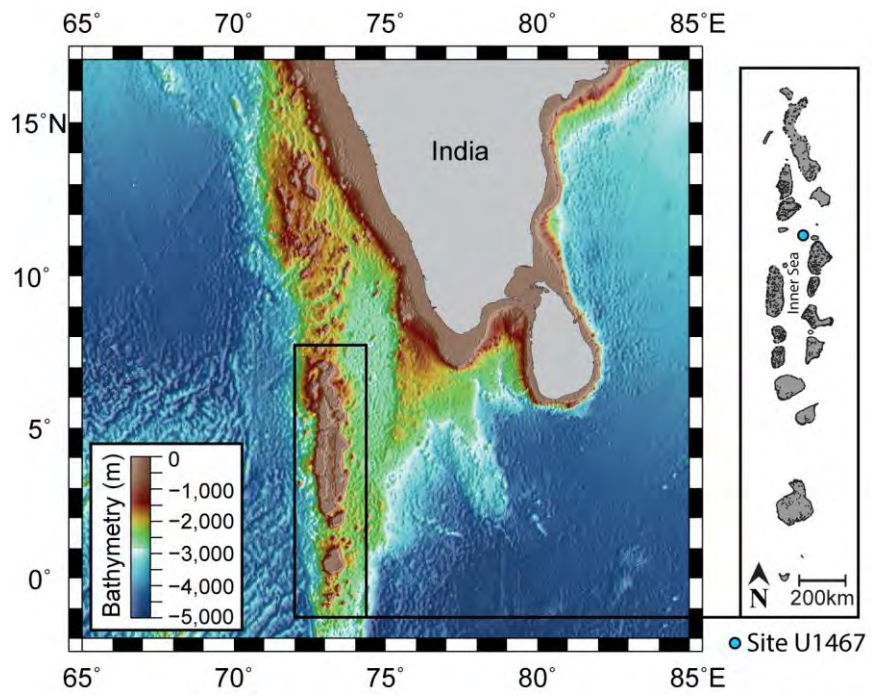


**Fig. 1.**

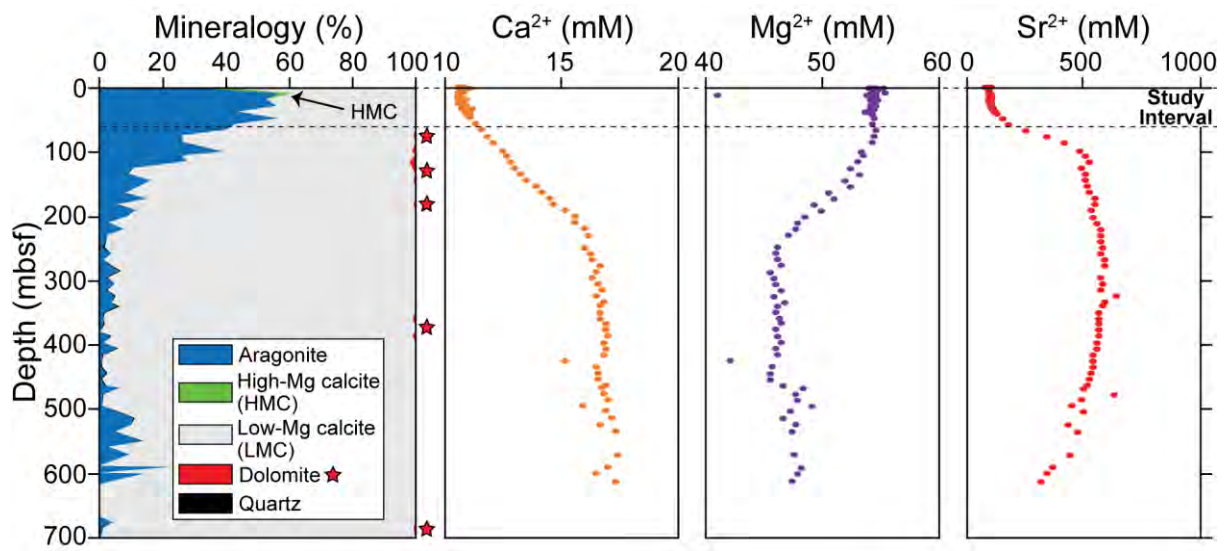
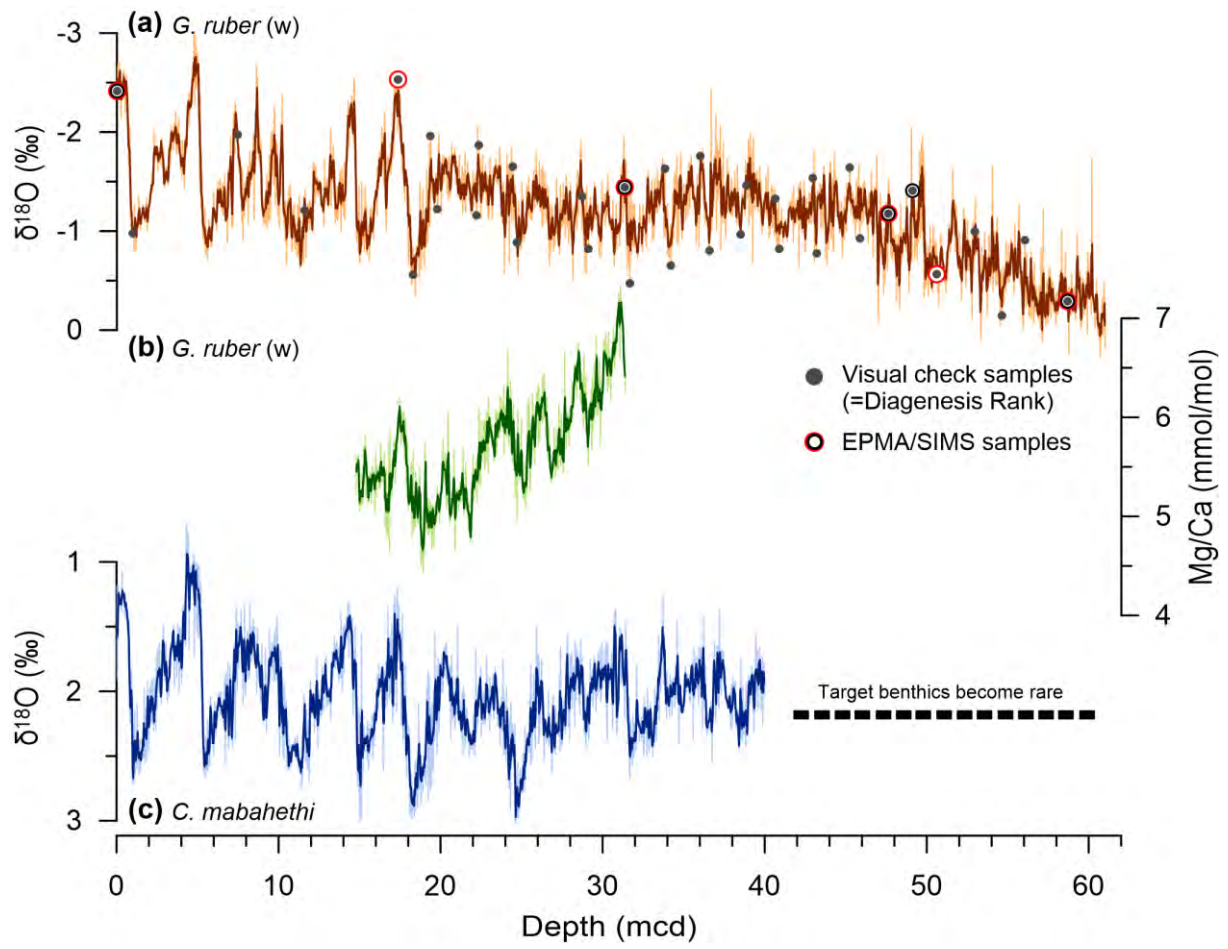


Fig. 2.



**Fig. 3.**



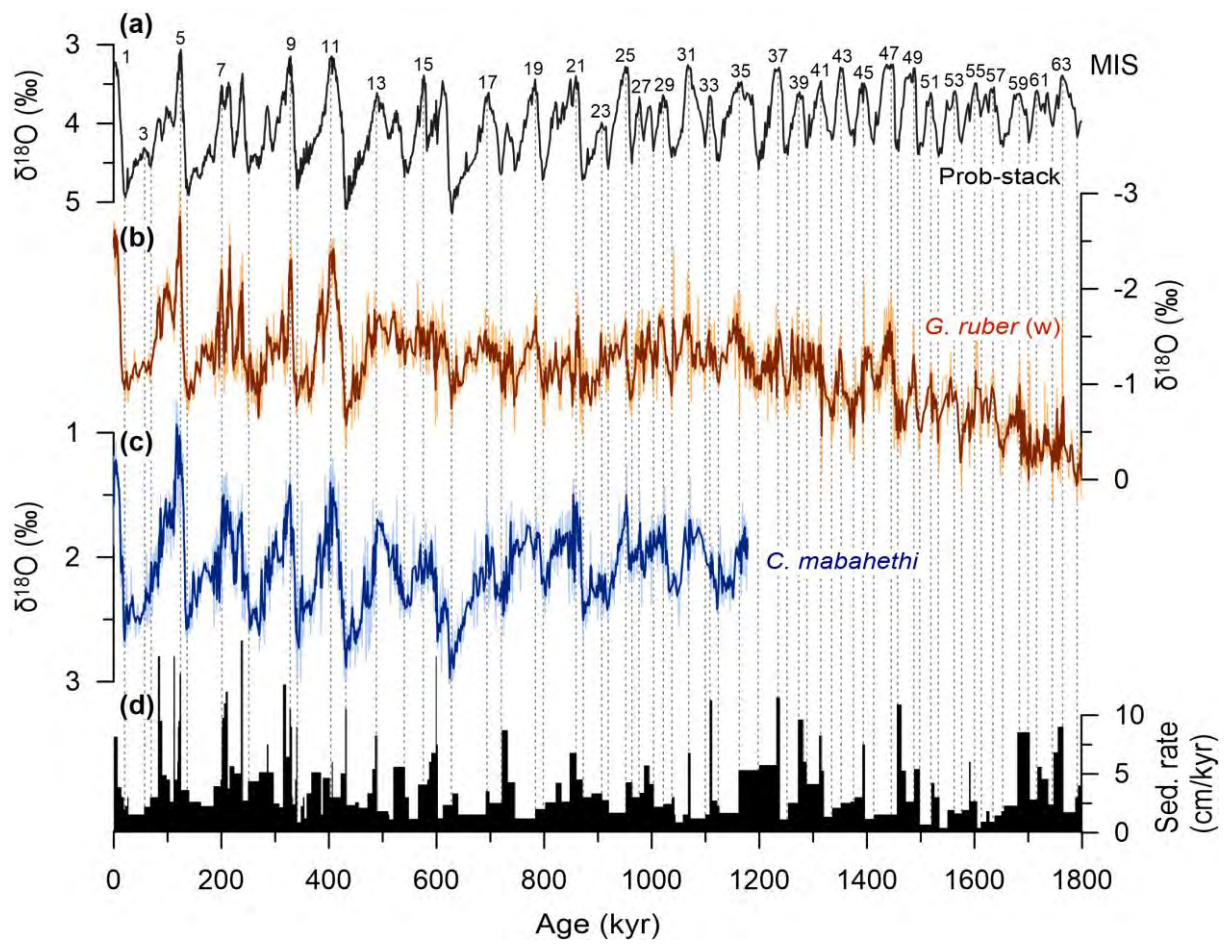


Fig. 4.

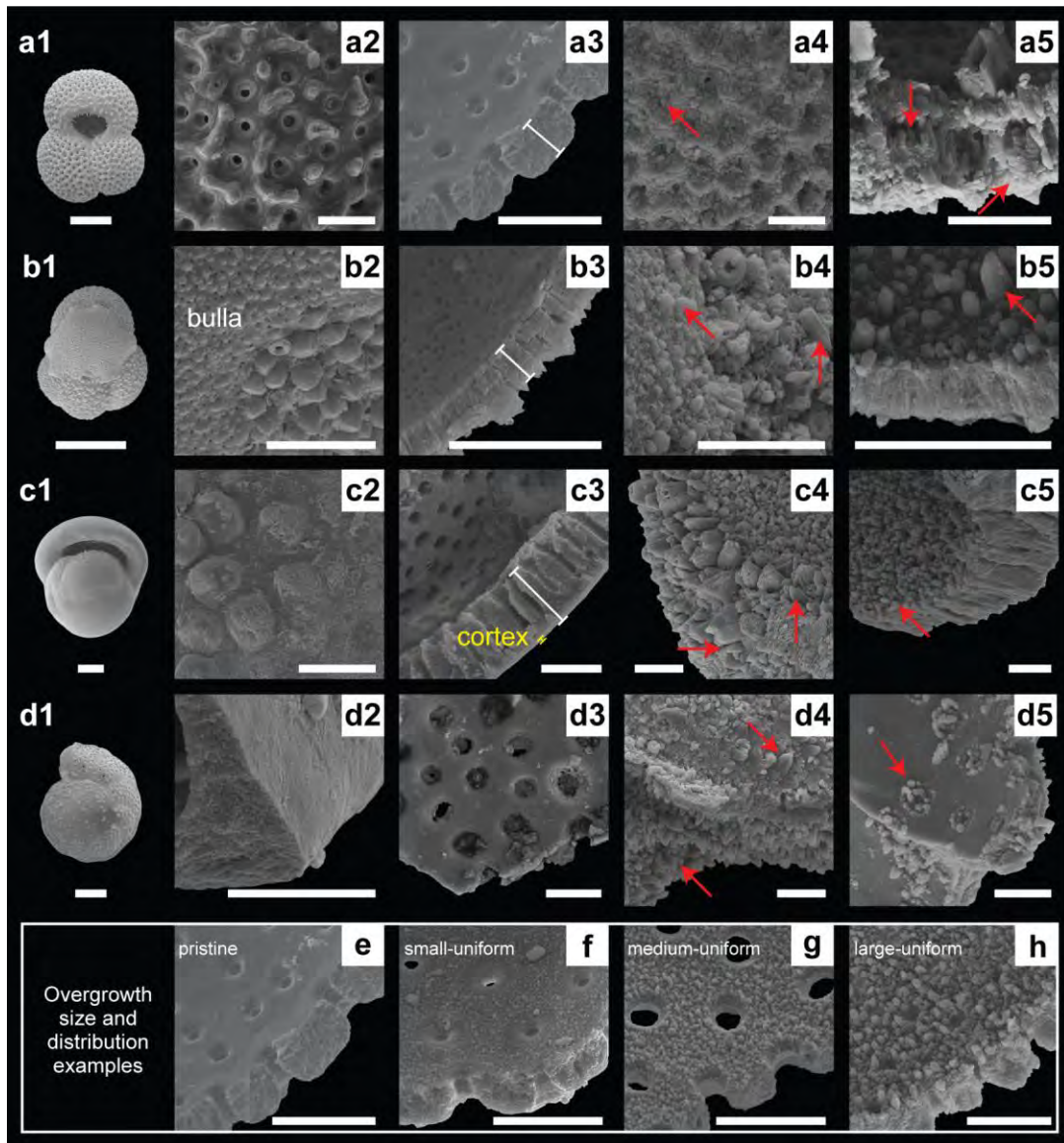
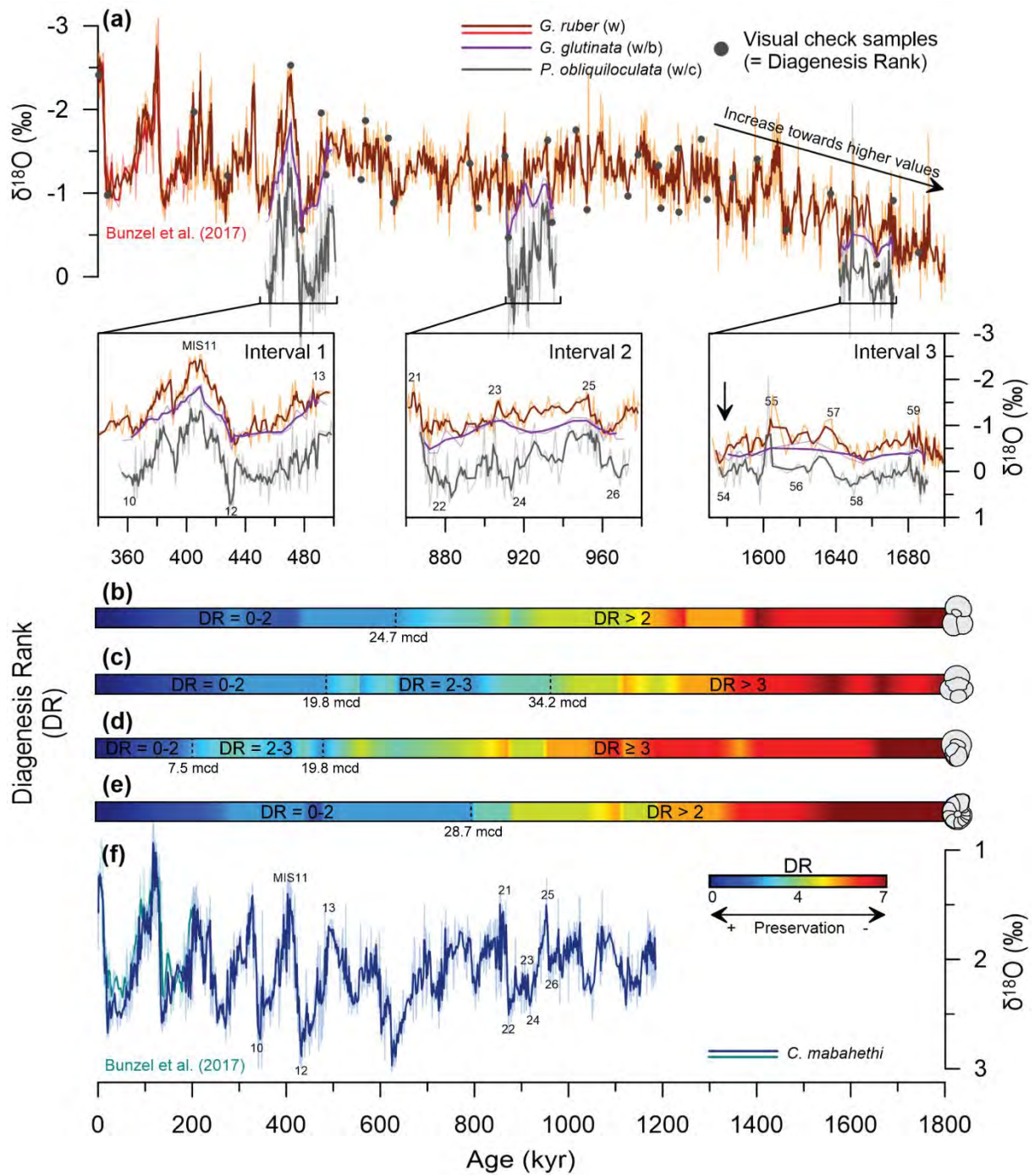
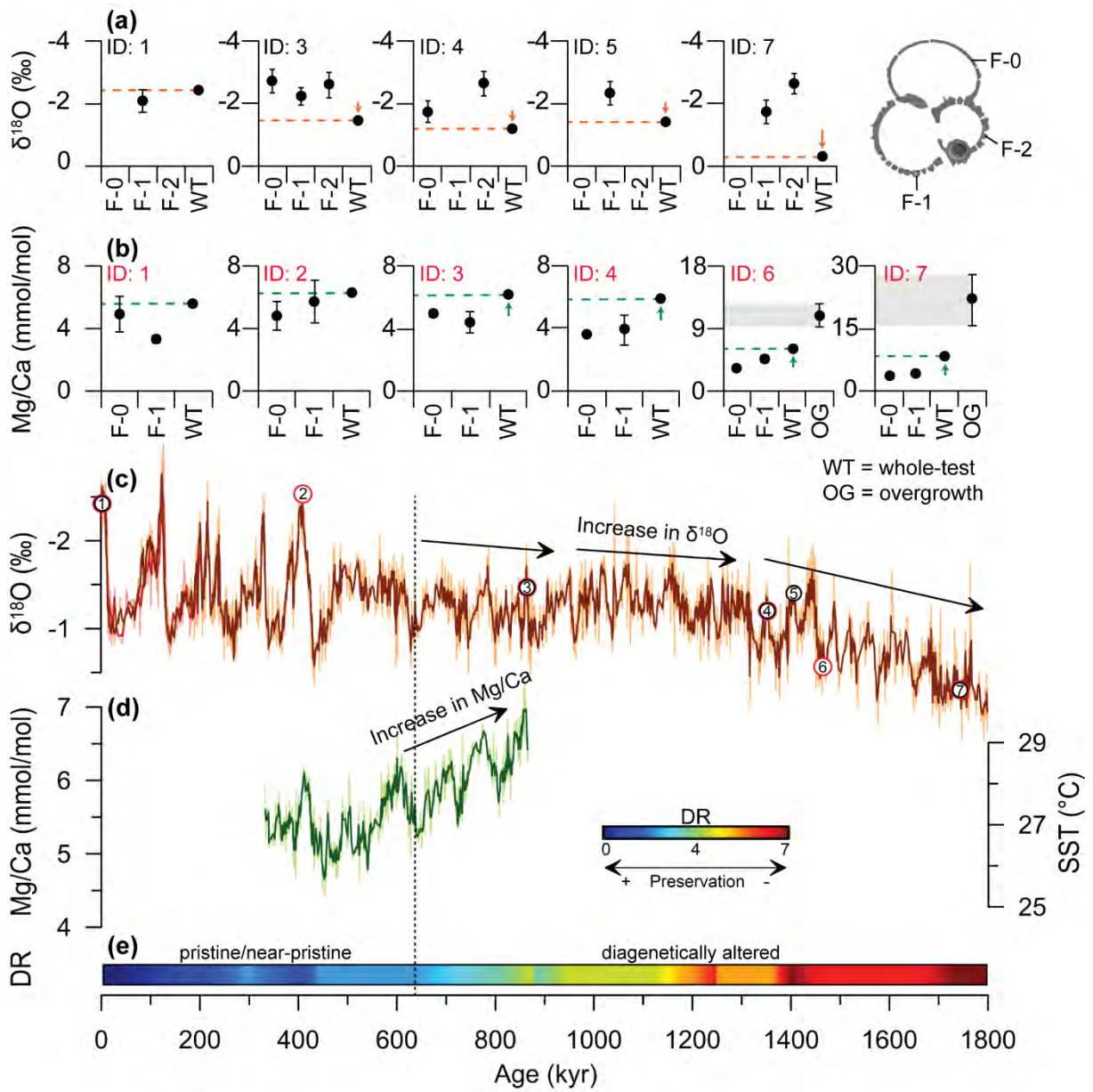


Fig. 5.



**Fig. 6.**



**Fig. 7.**

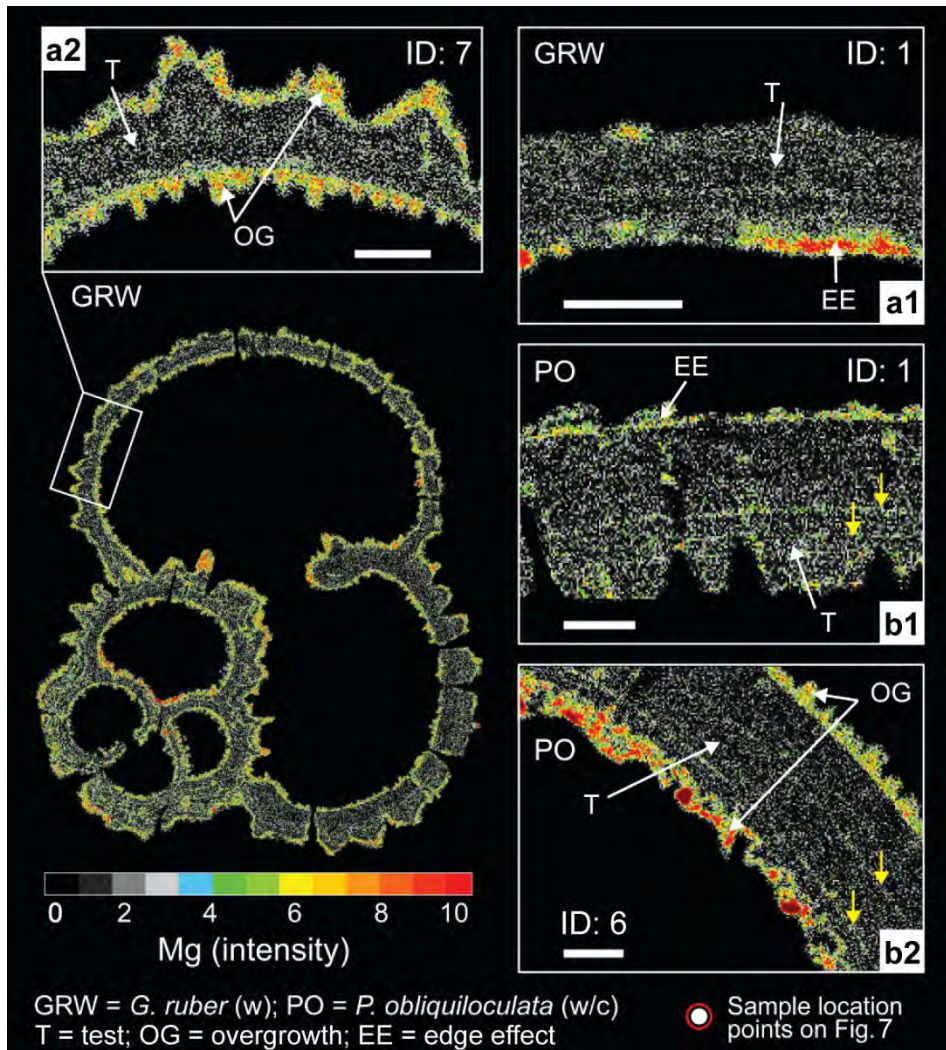


**Fig. 8.**

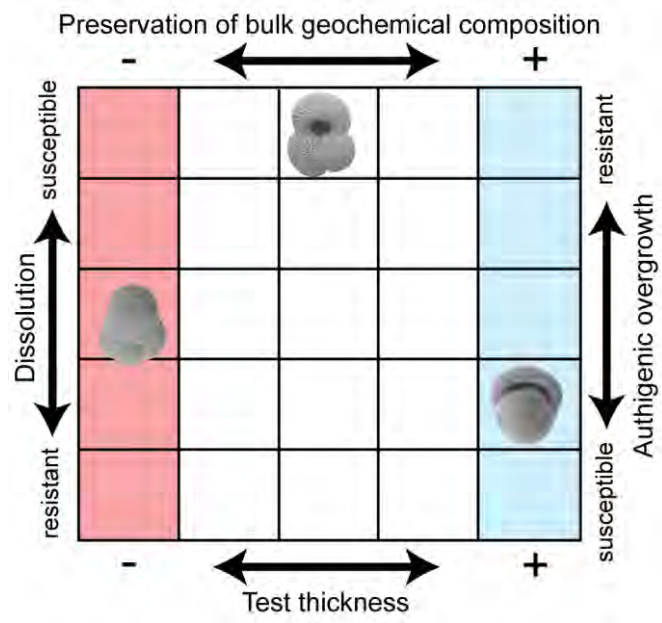


**Fig. 9.**

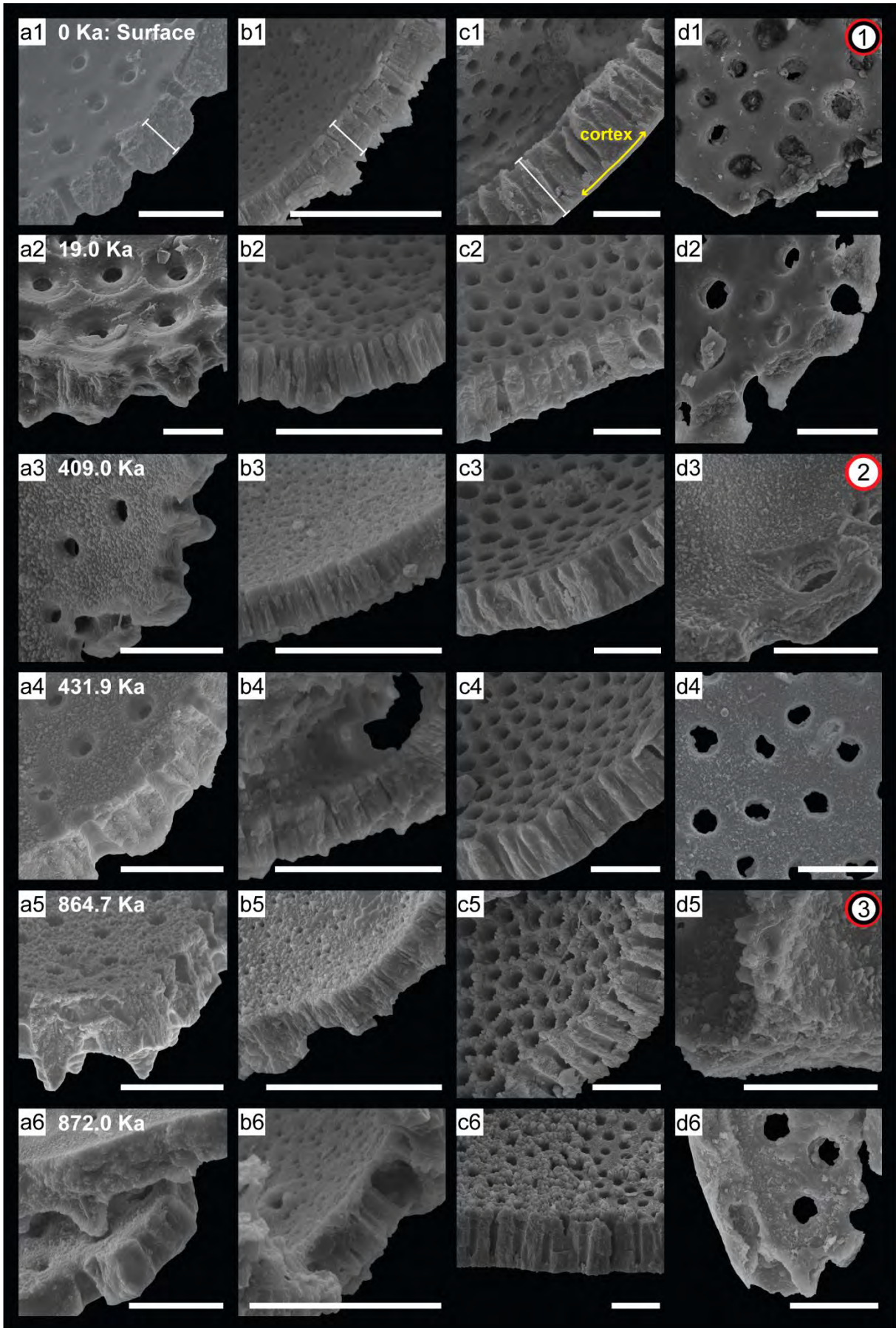
**Supplementary Material 1. Representative visual SEM images used to define the Diagenesis Rank (DR) values for the individual species from IODP Expedition 359 Site U1467.**

**Supplementary Figs. 1a–b.**

IODP Expedition 359 Site U1467 cross section and inner test surface SEM images of (a) *G. ruber* (w); (b) *G. glutinata* (w/b); (c) *P. obliquiloculata* (w/c) and (d) *C. mabahethi/wuellerstorfi* for Samples: (1) A, B-Mudline; (2) C-1H-1, 99-100 cm; (3) B-3H-3, 9-10 cm; (4) B-3H-3, 102-103 cm; (5) B-4H-5, 36-37 cm; (6) C-4H-3, 87-88 cm; (7) C-5H-4, 30-31 cm; (8) B-6H-2, 75-76 cm; (9) B-6H-3, 75-76 cm; (10) B-6H-4, 75-76 cm; (11) C-6H-5, 57-58 cm; (12) B-7H-3, 75-76 cm. For reference, SIMS and EPMA Samples 1-7 are indicated in the black and red circles, respectively. White bars indicate test thickness. Scale bars = 20  $\mu\text{m}$ .

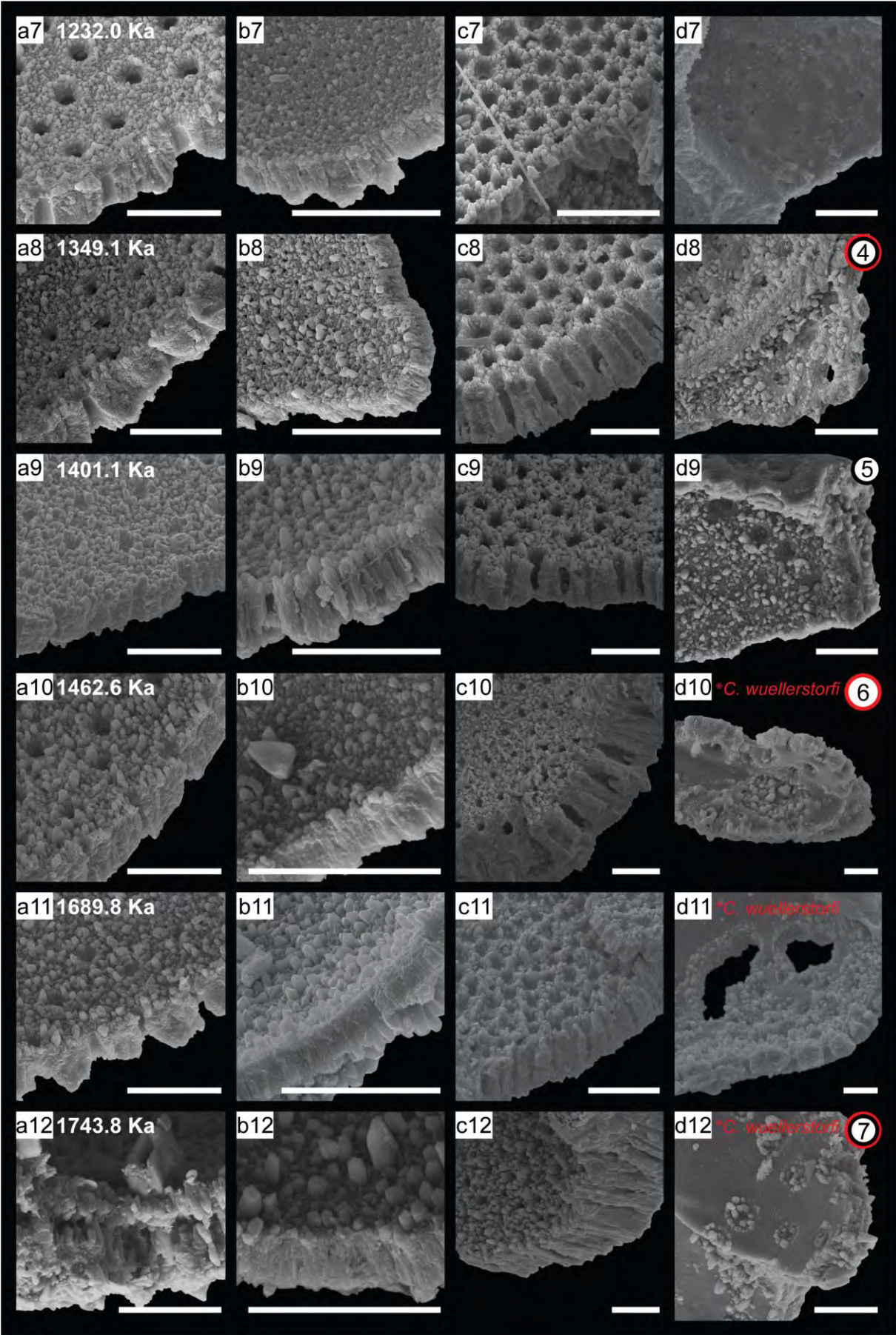
**Supplementary Figs. 1c–d.**

IODP Expedition 359 Site U1467 external test surface SEM images of (e) *G. ruber* (w); (f) *G. glutinata* (w/b); (g) *P. obliquiloculata* (w/c) and (h) *C. mabahethi/wuellerstorfi* for Samples: (1) A, B-Mudline; (2) C-1H-1, 99-100 cm; (3) B-3H-3, 9-10 cm; (4) B-3H-3, 102-103 cm; (5) B-4H-5, 36-37 cm; (6) C-4H-3, 87-88 cm; (7) C-5H-4, 30-31 cm; (8) B-6H-2, 75-76 cm; (9) B-6H-3, 75-76 cm; (10) B-6H-4, 75-76 cm; (11) C-6H-5, 57-58 cm; (12) B-7H-3, 75-76 cm. For reference, SIMS and EPMA Samples 1-7 are indicated in the black and red circles, respectively. Scale bars = 20  $\mu\text{m}$ .

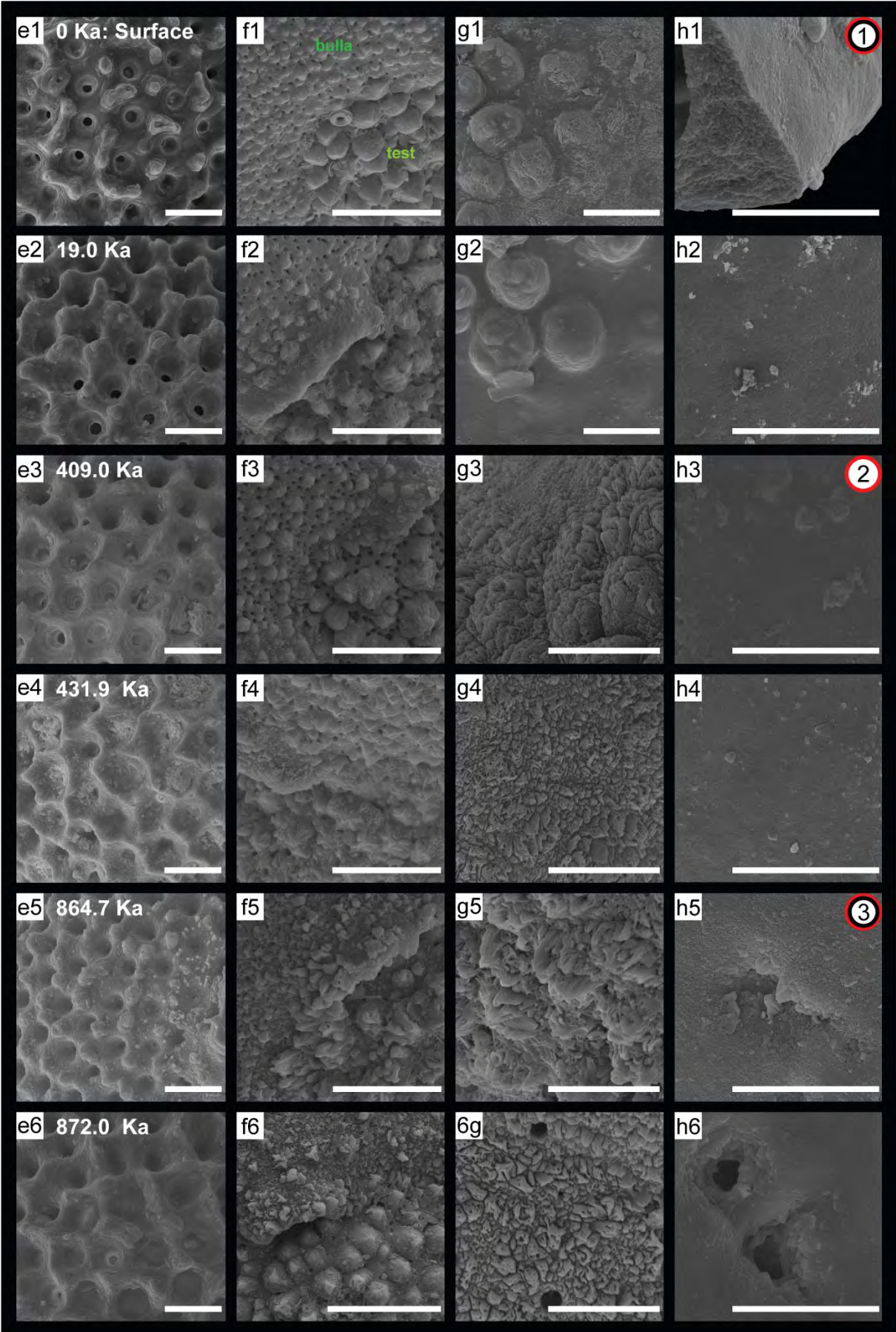


Supplementary Fig. 1a.

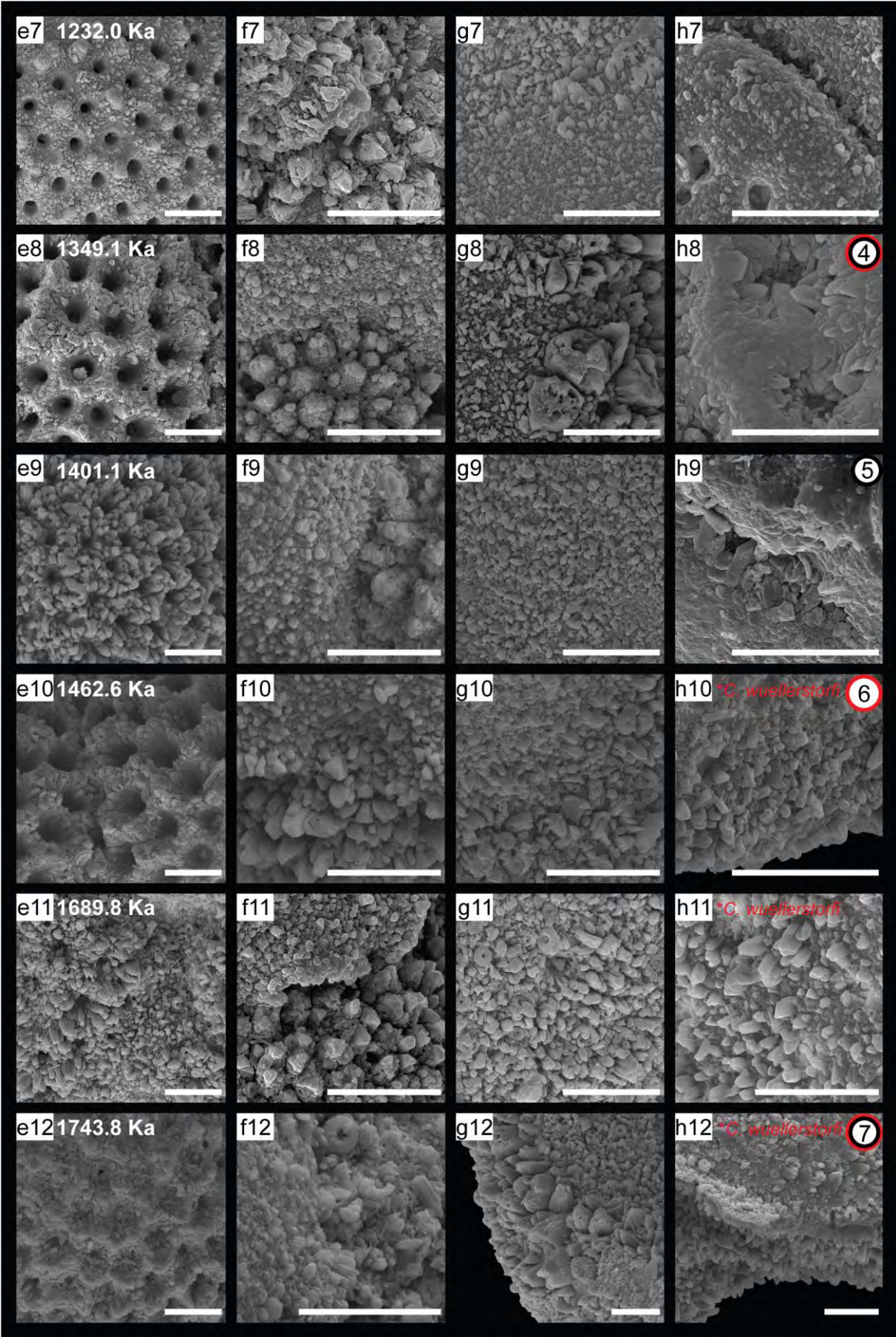




Supplementary Fig. 1b.

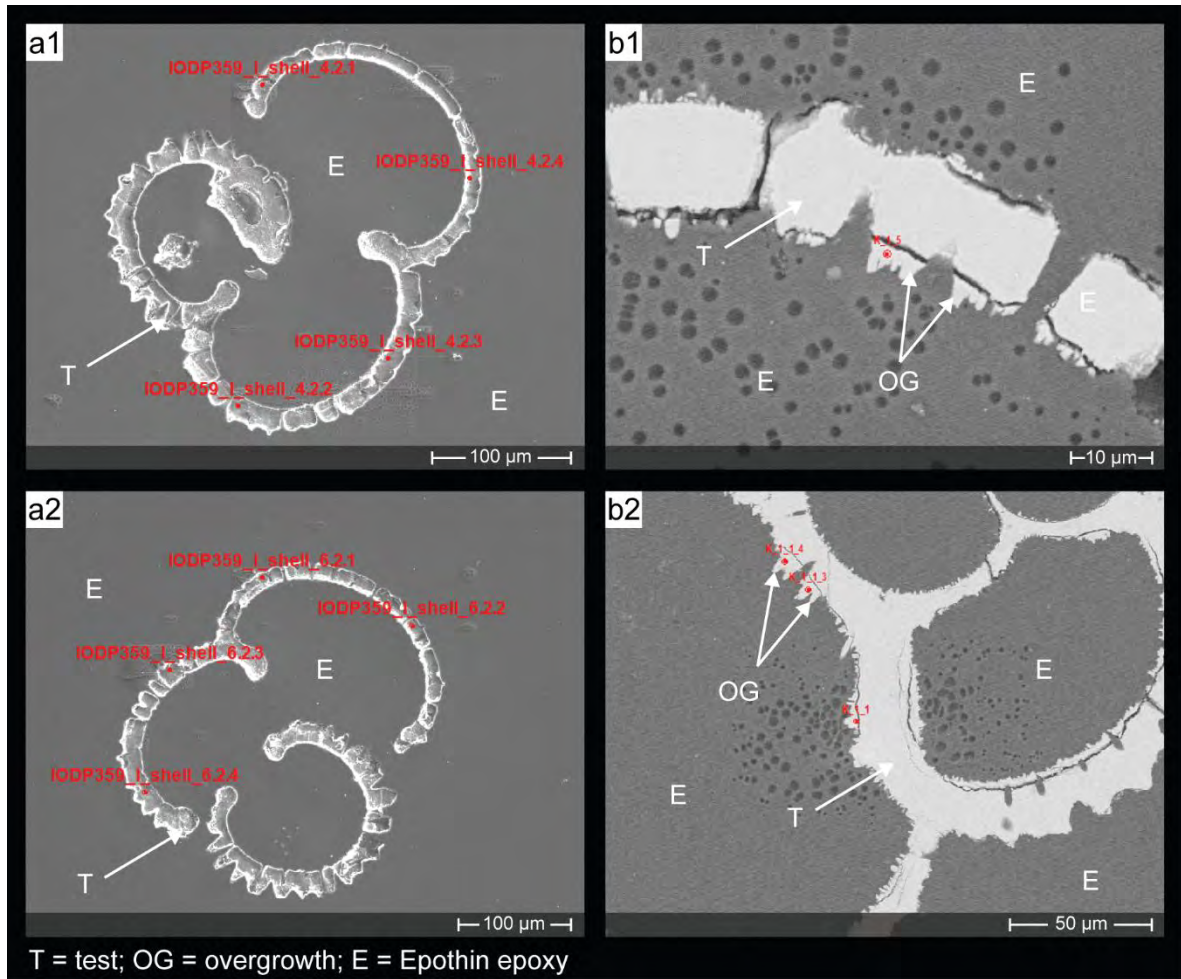


Supplementary Fig. 1c.



Supplementary Fig. 1d.

**Supplementary Material 2. Electron Probe Micro-Analyzer (EPMA) data.**



**Supplementary Fig. 2a.** IODP Expedition 359 Site U1467 *G. ruber* (w) SEM images showing examples of EPMA spot measurements for (a) the foraminifera test (T) and (b) large authigenic overgrowths (OG). Samples: (a1) B-4H-5, 36-37 cm; a2) B-6H-2, 75-76 cm; (b1-2) B-6H-4, 75-76 cm (Approximate location of the EPMA spots are shown for reference with the red dots with the red text indicating their individual EPMA IDs).

**Supplementary Table 2a.** IODP Expedition 359 Site U1467 *G. ruber* (w) EPMA test measurements used in the study. Measurements with total counts < 97 and > 102 were excluded.  
Note: SrO was measured for all samples and was zero in all instances.

Sample	EPMA ID	Sample ID	CaO	MgO	C	Total	Chamber	Mg/Ca (mmol/mol)
359-U1467B-Mudline	IODP359 I shell 1.1.1	1	56.45	0.21	44.53	101.19	F-0	5.17
359-U1467B-Mudline	IODP359 I shell 1.1.2		56.00	0.26	44.24	100.50	F-0	6.49
359-U1467B-Mudline	IODP359 I shell 1.2.3		55.23	0.19	43.55	98.97	F-0	4.87
359-U1467B-Mudline	IODP359 I shell 1.2.4		55.17	0.13	43.44	98.74	F-0	3.25
359-U1467B-Mudline	IODP359 I shell 1.1.3		55.86	0.13	43.98	99.97	F-1	3.17
359-U1467B-Mudline	IODP359 I shell 1.1.4		55.40	0.12	43.61	99.13	F-1	3.11
359-U1467B-Mudline	IODP359 I shell 1.2.2		55.74	0.15	43.91	99.80	F-1	3.70
359-U1467B-3H-3, 9-10 cm	IODP359 I shell 2.1.1	2	55.55	0.18	43.79	99.52	F-0	4.51
359-U1467B-3H-3, 9-10 cm	IODP359 I shell 2.1.2		56.30	0.26	44.47	101.03	F-0	6.43
359-U1467B-3H-3, 9-10 cm	IODP359 I shell 2.2.1		55.37	0.18	43.65	99.20	F-0	4.45
359-U1467B-3H-3, 9-10 cm	IODP359 I shell 2.2.2		55.41	0.16	43.66	99.23	F-0	3.90
359-U1467B-3H-3, 9-10 cm	IODP359 I shell 2.1.3		54.98	0.29	43.46	98.73	F-1	7.36
359-U1467B-3H-3, 9-10 cm	IODP359 I shell 2.1.4		54.82	0.24	43.28	98.34	F-1	6.14
359-U1467B-3H-3, 9-10 cm	IODP359 I shell 2.2.3		55.31	0.14	43.56	99.01	F-1	3.54
359-U1467B-3H-3, 9-10 cm	IODP359 I shell 2.2.4	54.71	0.23	43.18	98.12	F-1	5.83	
359-U1467B-4H-5, 36-37 cm	IODP359 I shell 4.1.2	3	54.96	0.21	43.36	98.53	F-0	5.20
359-U1467B-4H-5, 36-37 cm	IODP359 I shell 4.2.4		55.13	0.19	43.47	98.79	F-0	4.81
359-U1467B-4H-5, 36-37 cm	IODP359 I shell 4.1.3		55.01	0.20	43.39	98.60	F-1	5.15
359-U1467B-4H-5, 36-37 cm	IODP359 I shell 4.2.2		55.60	0.14	43.79	99.53	F-1	3.51
359-U1467B-4H-5, 36-37 cm	IODP359 I shell 4.2.3		55.75	0.18	43.95	99.88	F-1	4.48
359-U1467B-6H-2, 75-76 cm	IODP359 I shell 6.1.1	4	55.08	0.14	43.39	98.61	F-0	3.64
359-U1467B-6H-2, 75-76 cm	IODP359 I shell 6.1.3		55.17	0.13	43.44	98.74	F-1	3.32
359-U1467B-6H-2, 75-76 cm	IODP359 I shell 6.1.4		55.90	0.12	44.00	100.02	F-1	2.96
359-U1467B-6H-2, 75-76 cm	IODP359 I shell 6.1.5		55.75	0.15	43.92	99.82	F-1	3.79
359-U1467B-6H-2, 75-76 cm	IODP359 I shell 6.2.4		55.10	0.21	43.47	98.78	F-1	5.41
359-U1467B-6H-4, 75-76 cm	IODP359 I shell 8.1.2	6	56.90	0.13	44.79	101.82	F-0	3.11
359-U1467B-6H-4, 75-76 cm	IODP359 I shell 8.3.1		55.22	0.15	43.50	98.87	F-0	3.74
359-U1467B-6H-4, 75-76 cm	IODP359 I shell 8.1.4		55.32	0.16	43.59	99.07	F-1	4.08
359-U1467B-6H-4, 75-76 cm	IODP359 I shell 8.3.3		55.49	0.19	43.76	99.44	F-1	4.77
359-U1467B-6H-4, 75-76 cm	IODP359 I shell 8.3.4		54.92	0.22	43.34	98.48	F-1	5.53
359-U1467B-7H-3, 75-76 cm	IODP359 I shell 9.1.1	7	56.78	0.14	44.72	101.64	F-0	3.49
359-U1467B-7H-3, 75-76 cm	IODP359 I shell 9.1.2		55.74	0.15	43.90	99.79	F-0	3.66
359-U1467B-7H-3, 75-76 cm	IODP359 I shell 9.1.6		55.13	0.12	43.40	98.65	F-1	3.13
359-U1467B-7H-3, 75-76 cm	IODP359 I shell 9.2.3		55.09	0.18	43.43	98.70	F-1	4.43
359-U1467B-7H-3, 75-76 cm	IODP359 I shell 9.2.4		55.42	0.17	43.68	99.27	F-1	4.18
359-U1467B-7H-3, 75-76 cm	IODP359 I shell 9.2.5		54.66	0.17	43.08	97.91	F-1	4.33

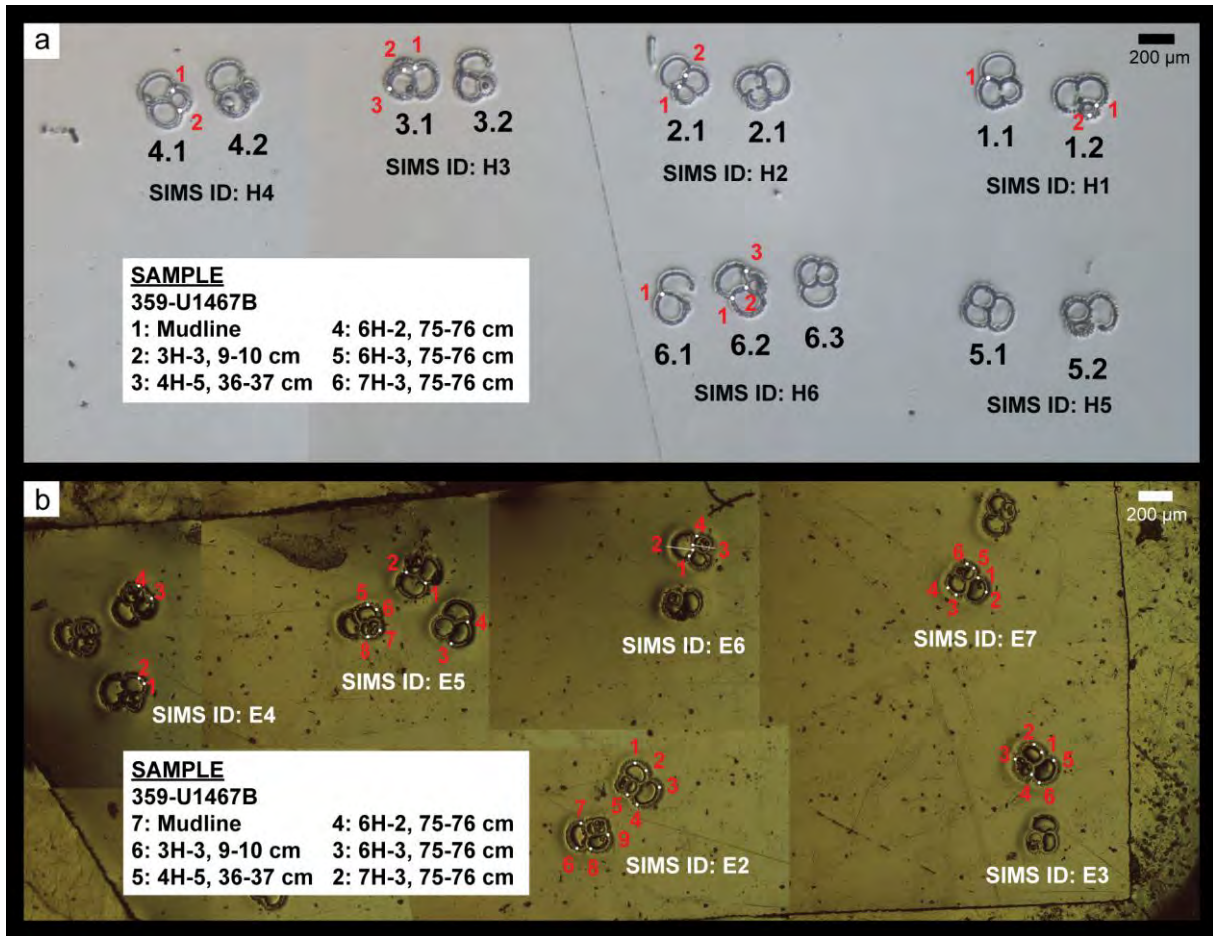
**Supplementary Table 2b.** IODP Expedition 359 Site U1467 *G. ruber* (w) EPMA overgrowth measurements used in the study. Measurements with total counts < 97 and > 102 were excluded. Note: SrO was measured for all samples and was zero in all instances.

Sample	EPMA ID	Sample ID	CaO	MgO	C	Total	Mg/Ca (mmol/mol)
359-U1467B-6H-4, 75-76 cm	K_1_1	6	54.70	0.55	43.52	98.77	13.87
359-U1467B-6H-4, 75-76 cm	K_1_1_4		56.29	0.41	44.62	101.32	10.13
359-U1467B-7H-3, 75-76 cm	K_5_2	7	56.19	0.53	44.67	101.39	13.12
359-U1467B-7H-3, 75-76 cm	K_5_2_b		54.80	1.05	44.15	100.00	26.71
359-U1467B-7H-3, 75-76 cm	K_5_1		54.76	1.01	44.08	99.85	25.76

**Supplementary Table 2c.** IODP Expedition 359 Site U1467 whole-test *G. ruber* (w) Mg/Ca data used in EPMA comparison. \*Data is taken from Stainbank et al. (2019).

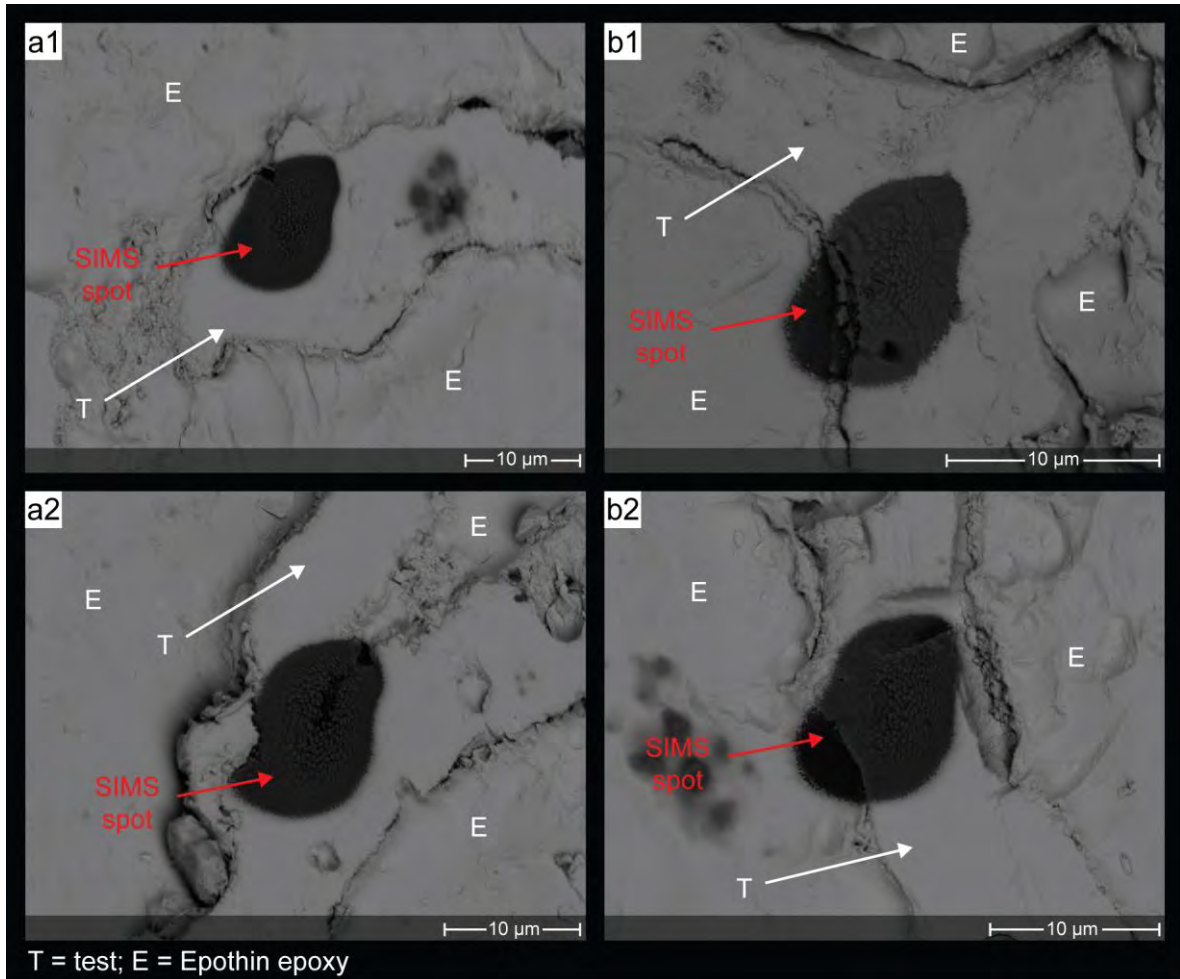
Sample	Sample ID	Mg/Ca (mmol/mol)
359-U1467B-Mudline	1	5.66*
359-U1467B-Mudline		5.65*
359-U1467B-3H-3, 9-10 cm	2	6.30
359-U1467B-3H-3, 9-10 cm		6.00
359-U1467B-3H-3, 9-10 cm		5.97
359-U1467B-4H-5, 36-37 cm	3	6.18
359-U1467B-4H-5, 36-37 cm		6.22
359-U1467B-6H-2, 75-76 cm	4	6.05
359-U1467B-6H-2, 75-76 cm		5.72
359-U1467B-6H-4, 75-76 cm	6	6.62
359-U1467B-6H-4, 75-76 cm		6.10
359-U1467B-7H-3, 75-76 cm	7	8.45
359-U1467B-7H-3, 75-76 cm		7.32

**Supplementary Material 3. Secondary Ion Mass Spectrometer (SIMS) data.**



**Supplementary Fig. 3a.** Compilation of IODP Expedition 359 Site U1467 (a) stereomicroscope images of embedded and polished *G. ruber* (w) SIMS Sample H showing approximate SIMS spot locations and (b) transmitted light microscope images of *G. ruber* (w) SIMS Sample E showing approximate SIMS spot locations. Sample IDs are indicated on the image.





**Supplementary Fig. 3b.** IODP Expedition 359 Site U1467 SEM images showing examples of *G. ruber* (w) SIMS spots which (a) hit only the foraminiferal test (T) and (b) which partly hit the epoxy (E). IODP Expedition 359 Site U1467 Samples: (a1) B-4H-5, 36-37 cm (SIMS ID:  $\delta^{18}\text{O}_{\text{foram\_H3\_1@1}}$ ); (a2) B-6H-2, 75-76 cm (SIMS ID:  $\delta^{18}\text{O}_{\text{foram\_H4\_1@1}}$ ); (b1) B-Mudline (SIMS ID:  $\delta^{18}\text{O}_{\text{foram\_H1\_2@1}}$ ); (b2) B-4H-5, 36-37 cm (SIMS ID:  $\delta^{18}\text{O}_{\text{foram\_H3\_1@3}}$ ).

**Supplementary Table 3a.** IODP Expedition 359 Site U1467 *G. ruber* (w) SIMS measurement spots, which hit no epoxy and were used in the study. (Session H-1 standard yield: 1.10E+09; Session E-2 standard yield: 9.30E+08). Bold indicates the SIMS spot, which hit substantial authigenic overgrowth.

Sample	SIMS ID	Sample ID	Session	Yield	$\delta^{18}\text{O}$ (‰)	2se (‰)	Chamber
359-U1467B-Mudline	$\delta^{18}\text{O}$ foram E7@4	1	E-2	1.021E+09	-2.08	0.35	F-1
359-U1467B-4H-5, 36-37 cm	$\delta^{18}\text{O}$ foram H3 1@1	3	H-1	1.093E+09	-2.70	0.38	F-0
359-U1467B-4H-5, 36-37 cm	$\delta^{18}\text{O}$ foram E5@6		E-2	8.728E+08	-2.22	0.29	F-1
359-U1467B-4H-5, 36-37 cm	$\delta^{18}\text{O}$ foram E5@7		E-2	9.644E+08	-2.14	0.39	F-2
359-U1467B-4H-5, 36-37 cm	$\delta^{18}\text{O}$ foram E5@8		E-2	9.468E+08	-2.81	0.30	F-2
359-U1467B-4H-5, 36-37 cm	$\delta^{18}\text{O}$ foram H3 1@2		H-1	1.043E+09	-2.82	0.50	F-2
359-U1467B-6H-2, 75-76 cm	$\delta^{18}\text{O}$ foram H4 1@1		4	H-1	1.049E+09	-1.75	0.35
359-U1467B-6H-2, 75-76 cm	$\delta^{18}\text{O}$ foram H4 1@2	H-1		1.065E+09	-2.63	0.38	F-2
359-U1467B-6H-3, 75-76 cm	$\delta^{18}\text{O}$ foram E3@1	5	E-2	1.078E+09	-2.15	0.34	F-1
359-U1467B-6H-3, 75-76 cm	$\delta^{18}\text{O}$ foram E3@2		E-2	9.996E+08	-2.51	0.43	F-1
359-U1467B-7H-3, 75-76 cm	$\delta^{18}\text{O}$ foram E2@1	7	E-2	9.859E+08	-1.55	0.44	F-1
359-U1467B-7H-3, 75-76 cm	$\delta^{18}\text{O}$ foram E2@2		E-2	9.881E+08	-2.18	0.39	F-1
359-U1467B-7H-3, 75-76 cm	$\delta^{18}\text{O}$ foram H6 1@1		H-1	1.045E+09	-2.00	0.26	F-1
<b>359-U1467B-7H-3, 75-76 cm</b>	<b><math>\delta^{18}\text{O}</math> foram H6 2@1</b>		<b>H-1</b>	<b>9.555E+08</b>	<b>-1.24</b>	<b>0.41</b>	<b>F-1</b>
359-U1467B-7H-3, 75-76 cm	$\delta^{18}\text{O}$ foram H6 2@2		H-1	1.025E+09	-3.15	0.38	F-2
359-U1467B-7H-3, 75-76 cm	$\delta^{18}\text{O}$ foram H6 2@3		H-1	1.035E+09	-2.12	0.27	F-2

**Supplementary Material 4. Table 4a. Age model data for IODP Expedition 359 Site U1467**

Tie-points

<b>359-U1467B, C Depth (mcd)</b>	<b>Prob-stack (Ahn et al., 2017) Age (kyr)</b>	<b>Sedimentation rate (cm/kyr)</b>
0.01	0	8.1
0.58	7	3.9
0.85	14	3.0
1.00	19	2.0
1.06	22	2.3
1.15	26	3.0
1.18	27	1.5
1.63	57	2.2
1.87	68	3.0
2.32	83	15.0
2.77	86	9.5
3.15	90	4.9
3.54	98	4.5
3.81	104	2.6
4.02	112	15.0
4.17	113	4.5
4.44	119	6.0
4.50	120	9.0
4.59	121	9.5
4.78	123	13.5
5.05	125	3.6
5.41	135	3.6
5.59	140	2.6
6.16	162	2.3
6.70	186	3.9
7.21	199	4.5
7.30	201	9.0
7.39	202	9.8
7.78	206	11.0
8.11	209	12.0
8.47	212	3.7
8.62	216	5.6
9.07	224	5.0
9.72	237	16.3
10.21	240	2.7
10.48	250	4.4
11.35	270	5.1
12.12	285	7.5
12.27	287	5.1
12.78	297	2.5
13.05	308	2.1
13.20	315	12.6
13.83	320	6.4
14.28	327	10.5
14.49	329	9.0
14.67	331	3.0

14.73	333	2.4
14.85	338	4.5
14.94	340	9.0
15.03	341	0.9
15.09	348	2.3
15.18	352	3.0
15.24	354	1.2
15.30	359	3.3
15.60	368	5.1
16.47	385	1.5
16.53	389	4.6
17.13	402	3.0
17.25	406	6.0
17.31	407	3.0
17.37	409	3.0
17.76	422	5.0
18.21	431	10.5
18.42	433	2.3
18.79	449	2.6
18.97	456	2.1
19.30	472	3.3
19.60	481	5.4
19.87	486	8.2
20.20	490	1.8
20.56	510	1.5
20.59	512	1.1
20.68	520	5.6
21.85	541	3.0
22.06	548	1.2
22.27	566	4.1
22.96	583	4.5
23.14	587	6.0
23.38	591	6.8
23.92	599	15.0
24.07	600	7.5
24.22	602	1.2
24.34	612	2.3
24.76	630	3.3
25.09	640	1.5
25.87	692	3.5
26.08	698	2.5
26.68	722	8.7
27.55	732	4.3
28.15	746	1.2
28.60	784	2.0
28.96	802	2.5
29.47	822	4.2
29.89	832	2.6
30.31	848	6.8
31.12	860	4.5

31.30	864	4.5
31.66	872	3.0
32.14	888	3.3
32.80	908	2.8
33.13	920	1.7
33.67	952	4.2
34.18	964	3.0
34.60	978	3.4
34.87	986	5.7
35.44	996	4.1
35.77	1004	2.2
36.16	1022	2.4
36.55	1038	3.0
36.67	1042	1.5
36.70	1044	0.9
36.82	1058	1.5
36.97	1068	6.8
37.24	1072	1.2
37.57	1100	1.5
37.69	1108	11.3
38.14	1112	2.7
38.41	1122	2.3
38.50	1126	1.7
39.10	1162	5.3
41.11	1200	5.7
42.94	1232	11.5
43.63	1238	1.1
43.81	1254	2.5
44.26	1272	9.6
45.22	1282	6.0
45.58	1288	4.1
46.57	1312	8.2
46.90	1316	5.3
47.11	1320	1.3
47.32	1336	2.1
47.65	1352	2.5
48.10	1370	2.6
48.31	1378	3.0
48.73	1392	7.5
49.03	1396	1.2
49.24	1414	1.5
49.72	1446	1.5
49.87	1456	10.9
50.74	1464	5.2
51.16	1472	2.6
51.58	1488	5.4
52.12	1498	0.7
52.27	1520	4.2
52.48	1525	3.0
52.78	1535	0.4

52.84	1550	1.9
53.08	1563	1.6
53.32	1578	1.9
53.56	1590	6.0
53.71	1593	2.6
54.04	1605	0.4
54.07	1613	0.9
54.16	1623	1.8
54.25	1628	0.9
54.34	1638	1.4
54.52	1650	1.8
54.61	1655	2.3
55.18	1680	8.5
57.10	1703	2.8
57.52	1718	5.6
57.94	1725	4.6
58.51	1738	2.4
58.75	1748	6.8
59.26	1755	9.0
60.16	1765	1.7
60.55	1788	3.0
60.70	1793	4.0
61.00	1800	3.4